Max-Planck-Institut
für Meteorologie

REPORT No. 253

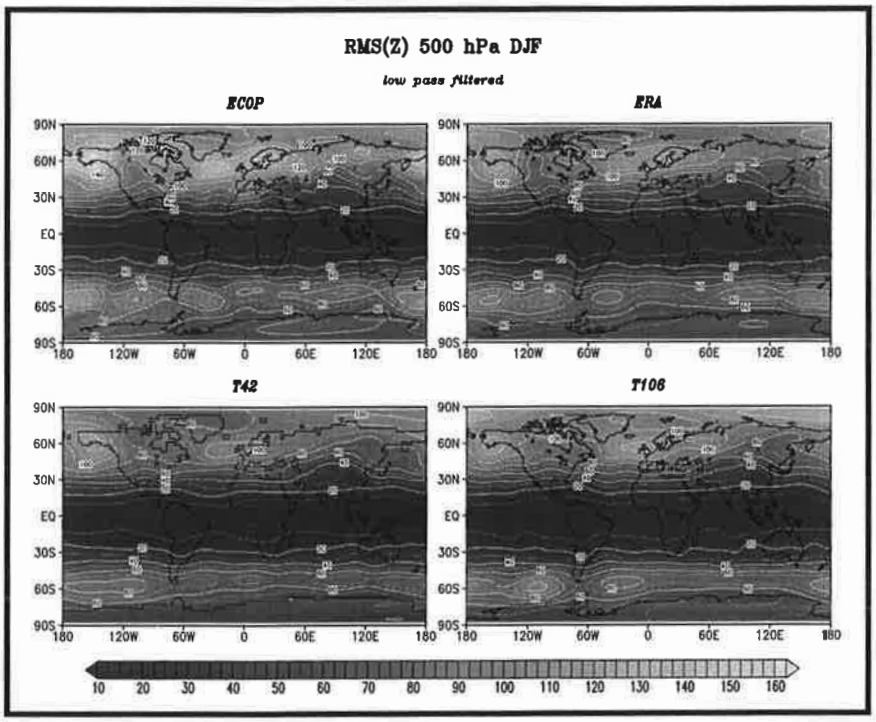

IMPACTS OF HORIZONTAL RESOLUTION ON SIMULATED CLIMATE STATISTICS IN ECHAM 4

by

Martin Stendel • Erich Roeckner

HAMBURG, March 1998

AUTHORS:

Martin Stendel,
Erich Roeckner

Max-Planck-Institut für Meteorologie
Hamburg
Germany

MAX-PLANCK-INSTITUT
FÜR METEOROLOGIE
BUNDESSTRASSE 55
D-20146 HAMBURG
F.R. GERMANY

Tel.: +49 - (0)40 - 411 73 - 0
Telefax: +49 - (0)40 - 411 73 - 298
E-Mail: <name>@dkrz.de

Impacts of horizontal resolution on simulated climate statistics in ECHAM 4

Martin Stendel and Erich Roeckner

Max-Planck-Institut für Meteorologie
Bundesstraße 55, 20146 Hamburg, Germany

ISSN 0937 - 1060

Abstract

The sensitivity of a general circulation model to changes in resolution is studied using the Max Planck Institute for Meteorology (MPI) 19-level model, ECHAM4. Simulations extending over a period between 10 and 15 years, with observed sea surface temperatures as lower boundary conditions from 1979 onward, have been performed using four different horizontal resolutions, T21, T30, T42 and T106. The atmospheric time-mean state and the intraseasonal variability are compared to the European Centre for Medium Range Weather Forecasts (ECMWF) reanalyses and a few other observational datasets.

The T30, T42 and T106 simulations are similar in many respects, whereas the T21 simulation is qualitatively different. Several effects related to model resolution could be identified, such as increasing tropical upper tropospheric warming with increasing resolution. This is due to more vigorous tropical convection, larger ice water content and, hence, increasing cirrus cloud greenhouse effect. Associated with this increasing warming at higher resolution is a poleward expansion of the zonally averaged circulation regime. On the other hand, the zonally asymmetric component of the circulation, i.e., the stationary waves, improve with higher resolution. Also, higher resolution has a positive impact on regional precipitation patterns which are affected by orography such as the summer monsoon precipitation over India.

Intraseasonal variability has been analyzed only for the higher resolution models, T42 and T106. Compared to the ECMWF reanalyses, both models are able to simulate the intraseasonal geopotential height variability, eddy fluxes of heat and momentum, and eddy kinetic energy with reasonable accuracy. This applies to transient eddies in both the bandpass and lowpass regime and to the stationary eddies as well.

Some biases can be identified which are more or less independent of resolution. These include the mislocation of the Azores high and the overestimation of its intensity, a cold bias in the polar upper troposphere and lower stratosphere and the poleward and upward displacement of the maxima of geopotential height variability, momentum fluxes and eddy kinetic energy.

An important finding is that the operational ECMWF analyses, which have been widely used for model validation, considerably overestimate the lowpass variability, as compared to the reanalyses, due to frequent changes of the forecast model and data assimilation scheme. This implies that the results from our investigations are not directly comparable to previous investigations that used operational analyses for validation.

1. Introduction

This study examines the sensitivity of a general circulation model (GCM) to changes in horizontal resolution. Discretization of the continuous mathematical equations is one of the error sources in numerical weather prediction models and GCMs. Another source is the parameterization of unresolved physical processes. However, since most of these parameterizations are resolution dependent, an increase in horizontal resolution will not only reduce the numerical truncation errors but also change the "model physics" in an unpredictable way so that the net effect could actually lead to a deterioration of the simulation. One example is the change of the momentum balance at mid-latitudes which leads to the well-known problem of "zonalisation" in high resolution models (Palmer et al., 1986). This problem is particularly evident in models which do not employ frictional dissipation through breaking gravity waves. If, on the other hand, this process is included in the model, the zonalisation problem becomes less pronounced (Boer and Lazare, 1988). As compared to observations, the studies by Mahlman and Umbscheid (1987), Boville (1991) and Boyle (1993) suggest some improvements with increasing resolution, whereas Kiehl and Williamson (1991) found a tendency for underestimating cloud cover in high resolution models. More recently, Déqué and Piedelievre (1995) have performed ten year AMIP (Atmospheric Model Intercomparison Project; Gates, 1992) simulations. They found that the winter time general circulation over the North Atlantic improves with increasing resolution.

In this study, we use data of a 10-year climate simulation at T106 resolution (about 100 km), which has recently been performed with the MPI general circulation model, ECHAM4 (Roeckner et al., 1996, henceforth referred to as R96). Additional experiments (15 years) were performed at coarser horizontal resolutions, i.e., T21, T30 and T42, respectively. In all cases, the model was forced with observed sea surface temperatures (SSTs). For the period 1979 to 1988, the so-called AMIP data set was used (Gates, 1992), and thereafter the SST data from NCEP/CAC (Reynolds, 1988). Since we have only 10 years of T106 simulation available, one may suspect that part of the differences between the model simulations shown later could be attributed to insufficient sampling. However, a comparison of two 10-year T42 realizations revealed the robustness of the climate statistics shown in this study. For model validation we generally use ECMWF reanalyses (ERA) available for the period 1979 to 1993 (Gibson et al., 1997). For the validation of precipitation, we refer to the so-called "GPCP Version 1 combined precipitation data set" (Huffman et al., 1995). In this analysis, gauge measurements are used where available. Over the oceans, infrared and microwave radiation observations monitored from satellites are used. The resolution is comparable to T42. High resolution precipitation forecast fields are available from ERA. However, since there are spinup and other problems with precipitation forecasts compared to observational estimates (Stendel and Arpe, 1997), the latter are preferred.

In this study we address the following questions:

1) Does the large-scale climate statistics change with increasing resolution in a systematic way?
2) To what extent does increasing resolution improve the simulated climate statistics?

In the following section, we briefly describe the ECHAM4 model. The time-mean state of basic climate variables is discussed in section 3, the intraseasonal variability due to both transient and stationary eddies is presented in section 4, and a few conclusions are drawn in section 5.

For convenience, coloured versions of the Figures presented in this report can be accessed via the World Wide Web at **http://www.mpimet.mpg.de/Deutsch/Reports/Bilder/Reports241-255/Rep253/Report253Figs.html**.

2. Model description and parameter choice

The present study has been performed with the ECHAM4 model which is described in detail in R96. For all simulations, the standard 19-level hybrid sigma-pressure coordinate system is used. The vertical domain extends up to the pressure level of 10 hPa. Prognostic variables are vorticity, divergence, temperature, specific humidity, the logarithm of surface pressure and the mixing ratio of total cloud water. Except for the water components, the prognostic variables are represented by spherical harmonics with triangular truncation at wavenumbers 21, 30, 42 or 106, respectively. A semi-implicit time stepping scheme is used together with a weak time filter. The time step for dynamics and physics is 40 min (at T21 resolution), 30 min (T30), 24 min (T42) or 15 min (T106), respectively. The radiation time step is 2 hours, independent of resolution. Both seasonal and diurnal cycles in solar forcing are simulated. The three-dimensional transport of water vapour and cloud water is calculated by using a semi-Lagrangean scheme (Williamson and Rasch, 1994).

Horizontal diffusion is expressed in the form of a hyper-Laplacian, with $n > 1$, which essentially confines the damping to the high-wavenumber end of the spectrum. To avoid fictitious reflection at the upper boundary, a high-diffusion sponge zone is realized through a gradual decrease of the order of the scheme in the lower stratosphere. The *e*-folding diffusive decay time at the highest resolvable wave number is independent of height but varies with resolution (see below). The diffusion operator is applied to vorticity, divergence and temperature, but not to the water components which are advected by the semi-Lagrangean scheme.

The turbulent surface fluxes are calculated from the Monin-Obukhov similarity theory (Louis, 1979). Within and above the atmospheric boundary layer, a higher-order closure scheme is used to compute the turbulent transfer of momentum, heat, moisture and cloud water. The eddy diffusion coefficients are calculated as functions of the turbulent kinetic energy E which is obtained

from the respective rate equation (Brinkop and Roeckner, 1995), including turbulent transport of E, generation/destruction by wind shear and buoyancy flux, and dissipation (but neglecting advection of E). The interaction between cloud and turbulence is represented by processes such as the vertical exchange of turbulent kinetic energy generated through radiative cooling at cloud top, the impact of cloud water on the buoyancy flux, and cloud top entrainment through the turbulent flux of cloud water.

Gravity wave drag associated with orographic gravity waves is simulated after McFarlane (1987) and Palmer et al. (1986), as modified by Miller et al. (1989), using directionally dependent subgrid-scale orographic variances obtained from a high-resolution dataset. Surface stress due to gravity waves excited by stably stratified flow over irregular terrain is calculated from linear theory and dimensional considerations. The surface wave stress is a function of low-level wind, orographic variance and buoyancy frequency. In addition, high-drag states are considered when the flow becomes hydraulic at low levels due to the breaking of lee waves. The vertical profile is calculated from a local wave Richardson number which describes the onset of turbulence due to convective instability and the turbulent breakdown approaching a critical level.

The soil model comprises the budgets of heat and water in the soil, the snow pack over land and the heat budget of land ice. Vegetation effects such as the interception of rain and snow in the canopy and the stomatal control of evapotranspiration are parameterized in a highly idealized way. The local runoff scheme is based on catchment considerations and takes into account subgrid-scale variations of field capacity over inhomogeneous terrain. A new dataset of mean land surface parameters such as background albedo, roughness length, vegetation type, leaf area index and soil parameters like water holding capacity, heat capacity and thermal conductivity has been compiled for ECHAM4 (Claussen et al., 1994), consistent with the Olson et al. (1983) definition of ecosystem complexes.

The parameterization of cumulus convection (shallow, mid-level and deep) is based on the bulk mass flux concept of Tiedtke (1989). However, according to the suggestions of Nordeng (1994), organized entrainment is related to buoyancy instead of moisture convergence, organized detrainment is computed for a spectrum of clouds detraining at different heights, and an adjustment-type closure is used for deep cumulus convection instead of the moisture convergence closure applied in the Tiedtke scheme. Moreover, the water loading is considered in the buoyancy calculation and the cloud water detrained at the top of cumulus clouds is entering as a source term in the stratiform cloud water equation. Also, different from the Tiedtke scheme, the physics of the stratocumulus regime is part of the boundary layer scheme.

The stratiform cloud water content is calculated from the respective budget equation including sources and sinks due to phase changes and precipitation formation due to coalescence of cloud droplets and gravitational settling of ice crystals. The convective cloud water detrained at the top of cumulus clouds is used as a source term in the stratiform cloud water equation. The for-

mation of thin maritime stratus forming under a low-level inversion is favoured by accounting for subgrid-scale cloudiness in the vertical, realized through a reduction of condensation threshold and saturation limit below the inversion.

The radiation code has been adopted from the ECMWF model (Fouquart and Bonnel, 1980; Morcrette et al., 1986) with a few modifications like the consideration of additional greenhouse gases (methane, nitrous oxide and 16 CFCs), the 14.6 μm band of ozone and various types of aerosols (optionally). Moreover, the water vapour continuum has been revised to include temperature weighted band averages of e-type absorption and also a band dependent ration of (p-e)-type to e-type continuum absorption (Giorgetta and Wild, 1995). The single scattering properties of cloud droplets and ice crystals are derived from the Mie theory with suitable adaptation to the broad-band model (Rockel et al., 1991), and the effective radius of droplets and ice crystals is parameterized in terms of the liquid and ice water content, respectively (Roeckner, 1995).

For the comparison of model simulations at different horizontal resolutions one can follow two strategies. The first one does not involve model tuning whatsoever, i.e., the free parameters in the physical parameterizations are chosen independently of resolution. The advantage of this approach is that differences in the results are due to changes in horizontal resolution alone. However, as discussed above, the simulated climate statistics does not only depend on numerical accuracy but also on parameterized physics including the parameter choice. These parameters are not universal, and a certain choice may be more favourable for one resolution than for the others so that a comparison between simulated and observed climate statistics may be misleading.

The other strategy does involve model tuning by choosing the optimal set of parameters at the respective resolution. This approach allows for a fair comparison of the simulated climate statistics with the observed one. However, due to the nonlinearity of the model equations, the optimization problem cannot be solved in a unique and objective way. In practice, a large number of test runs is required, and a cheap low resolution model can easier be optimized than an expensive high resolution one. In any case, a subjective assessment during model experimentation is required.

In this study, we have applied the second approach but model tuning is limited to a few processes which turned out to be extremely scale dependent such as frictional dissipation and precipitation formation (Table 1). For example, the surface wave stress exerted by flow over irregular terrain is a function of low-level wind, buoyancy frequency and subgrid-scale orographic variance which decreases with increasing resolution. This formulation also includes a free parameter which has to be determined empirically. In fact, it turned out that very low resolution models (like T21) perform best (for the wrong reasons, admittedly) without the gravity drag parameterization (Roeckner et al., 1992, henceforth R92). For similar reasons, the surface roughness parameter over the oceans (the so-called Charnock constant) is reduced in the T21 model

Table 1: Resolution dependence of certain parameters in the ECHAM4 model

Physical parameterization	Reference	T21	T30	T42	T106
Gravity wave drag					
Surface wave stress factor [10^{-5} m^{-1}]	R92, eq. 3.3.4	0.0	1.0	2.5	3.0
Surface fluxes over the ocean					
Charnock constant	R96, eq. 10	0.018	0.032	0.032	0.032
Horizontal diffusion					
e-folding decay time scale [hours] at highest resolvable wavenumber and order of operator	R96, eq. 3	6h ∇^{20}	12h ∇^{10}	9h ∇^{10}	3h ∇^{8}
Stratiform clouds					
Factor governing the efficiency of rain formation [10^{-4} s^{-1}]	R96, eq. 61	1.0	1.5	2.0	2.5
Factor governing the fall velocity of ice crystals	R96, eq. 62	1.65	1.84	1.97	2.14
Deep convection					
Relaxation time [hours] for adjustment closure	R96, eq. 50	2	1	1	1

compared to the other models. Finally, in the horizontal diffusion scheme, the order of the operator, or scale selectivity, increases with decreasing resolution, leaving the baroclinic waves largely unaffected, even at T21 resolution.

Similar to dissipation, the balance between cloud water sources (condensation) and sinks (precipitation formation) is extremely scale dependent. With the same set of parameters, high-resolution models tend to store more cloud water in the atmosphere than low-resolution models while variables like cloud cover or precipitation depend less on resolution. In order to keep the global mean cloud water content and radiation fluxes similar at all resolutions, and similar to observations as well, the parameters which determine the efficiency of precipitation formation and, hence, cloud lifetime have been adjusted (Table 1). As a result (Table 2), the top-of-atmosphere radiation fluxes at different resolutions are similar and, moreover, the differences between the simulated fluxes and ERBE analyses are within the range of observational uncertainty.

In general, the integration time is 15 years (1979 to 1993), except for T106 which has been run for 10 years only (1979 to 1988). The model history is written every 12 hour, and the results presented below are seasonal averages for December, January, February (DJF) and June, July, August (JJA), respectively.

Table 2: Global annual mean radiation fluxes [W m^{-2}] at the top of the atmosphere.
SW = absorbed solar radiation, LW = outgoing longwave radiation, NET = SW - LW.
ERBE stands for Earth Radiation Budget Experiment (Hartmann, 1993).

	T21	T30	T42	T106	ERBE
SW (clear sky)	286.5	286.4	286.2	286.6	288
SW (clear+cloudy)	236.3	237.1	236.9	236.5	240
SW (cloud forcing)	-50.2	-49.3	-49.3	-50.1	-48
LW (clear sky)	262.5	263.5	264.0	265.7	264
LW (clear+cloudy)	233.3	234.8	235.3	235.2	234
LW (cloud forcing)	29.2	28.6	28.7	30.5	30
NET (clear+cloudy)	3.1	2.3	1.6	1.3	6

3. Atmospheric time-mean state

In this section, the simulated time-mean state is compared with ERA. To allow for a better interpretation of the results, we decompose the atmospheric field variables into the zonally averaged component and into the zonally asymmetric, or stationary wave, component which is obtained by subtracting the zonal averages from the respective field variable.

3.1 Sea level pressure

Fig. 1 shows the meridional distributions of the zonally averaged sea level pressure for DJF and JJA, respectively. It is clearly visible that T21 is unrealistic regardless of season, especially in the Southern Hemisphere (SH) where the strength of the main pressure systems such as the subtropical high and the subpolar trough around Antarctica is much too weak and the position shifted equatorward compared to ERA. The other models are much more realistic in these respects but all of them tend to underestimate the subpolar trough in JJA. There is a distinct resolution dependence in the SH, i.e., both the subtropical high and the subpolar trough are becoming more pronounced with higher resolution so that the pressure gradient between these two systems is increasing with resolution. Moreover, not only the amplitude of the pressure systems depends on resolution but also their position, i.e., the pressure systems tend to move poleward with increasing resolution. In the Northern Hemisphere (NH), the most systematic resolution dependence is found over the Arctic where, as over Antarctica, the sea level pressure is becoming lower, and more realistic, with increasing resolution. In the NH mid-latitudes, the resolution dependence is not as obvious as in the SH. In DJF, position and strength of the subtropical high slightly degrade with higher resolution. In JJA, the intermediate resolution models (T30, T42) are closer to ERA than the T106 model. In both seasons, and at all resolutions, the equatorial trough is slightly too deep.

The geographic distribution of mean sea level pressure, shown in Fig. 2, yields some systematic features. The intensity of the Icelandic low in DJF is slightly underestimated at all resolutions. According to ERA, the core of the Icelandic low is between Greenland and Iceland. With increasing resolution, it moves from a position slightly westward of the observed one, at T30 resolution, to a position eastward of the observed one, halfway between Iceland and Norway, in the T106 model. Associated with this eastward shift of the core region is relatively low pressure over Europe so that the geostrophic flow across the North Atlantic becomes more zonal, at both T42 and T106 resolution, than in ERA. In the North Pacific, on the other hand, the resolution dependence is less obvious, i.e., the Aleutian low is simulated reasonably well at all resolutions. As in previous versions of ECHAM (c.f., R92), the strength of the Azores high in DJF is overestimated at all resolutions, except for T21, and its position is simulated too far northeast. In JJA, the pressure distribution is reasonably well captured by all of the models. The stationary wave errors are shown in Fig. 3. The error patterns are similar in shape, but the amplitudes, as expressed in terms of root mean square error (rmse), reduce with increasing resolution. In general, the error reduction is more systematic in the SH than in the NH and also more evident in JJA than in DJF.

3.2 Geopotential height

In the meridional profiles of zonal mean 500 hPa geopotential height, differences between the low and high resolution simulations are relatively small (Fig. 4). One exception, again, is the T21 simulation which shows unrealistic features in the extratropics of both hemispheres and too high geopotential over Antarctica, which is consistent with the surface pressure error pattern discussed above. At low latitudes, the geopotential height is overestimated in all models, but the errors slightly increase with increasing resolution. In conjunction with the underestimation of the tropical sea level pressure mentioned above, this has to be interpreted as an overestimation of tropical deep-layer temperature (see below). The stationary wave errors of the 500 hPa geopotential are displayed in Fig. 5. The error patterns are similar to those of mean sea level pressure (c.f., Figs. 2b, 3b), and not very different among the models themselves. However, as for sea level pressure, the amplitudes are systematically reduced with increasing resolution.

3.3 Temperature

A cold bias in the polar upper troposphere and lower stratosphere can be found in virtually all of the contemporary GCMs, regardless of model formulation (Boer et al., 1992) and horizontal resolution (Déqué et al., 1994). This is also the most prominent error in all of the ECHAM4 simulations (Fig. 6). On the other hand, the tropical and subtropical upper troposphere is too warm compared to ERA. This warm bias increases with resolution and reaches 4 K in JJA at T106 resolution. Since tropical temperatures are overestimated and polar temperatures are underestimated in the upper troposphere, there is a general tendency for overestimating the temperature gradient between the equator and the poles. Another suspicious feature is the summer warming over the Arctic which is most evident in the T106 simulation. The error patterns in the stationary wave component of temperature are shown in Fig. 7 for the 850 hPa level. Over the oceans,

where SST is prescribed, the errors are generally below 1 K. The errors are larger over land. As for the variables discussed earlier, the error patterns are almost independent of resolution but the amplitudes decrease with increasing resolution. As to be expected, the temperature of near-surface air depends crucially on the height of orography. As an example, Fig. 8a shows the orography at the different resolutions for the European area, and the near-surface (2m) temperature for this area is given in Figs. 8b,c. While there is hardly any orographic impact on 2m temperature at T30 resolution, orographic details are evident in the T106 simulation although the orographic impact is still smaller than in ERA, especially in DJF. For most parts of Europe, the JJA temperature in the T106 model is a few degrees too high.

3.4 Wind

Fig. 9 shows latitude-pressure cross sections of the zonal wind component for DJF and JJA, respectively. As pointed out by several authors (e.g., R96), one of the major wind errors in ECHAM4 is a mislocation of the jet maxima in the SH. This error increases with resolution. In JJA, there is no clear separation between the Antarctic night jet, which is located too far equatorward, and the subtropical jet, which is shifted upward by about 50 hPa. In the NH, the jet maxima are located at the correct position but shifted upward as in the SH. From the zonal wind errors shown in Fig. 10 some characteristic patterns can be identified. The upward and poleward shift of the jets discussed above can be identified, in all models, by a positive anomaly centered at the 100 hPa level. On the other hand, all models show a tropical upper tropospheric westerly wind error, but its magnitude is systematically decreasing with increasing resolution. At T21 resolution, there is a gross underestimation of the mid-latitude zonal wind, in particular in the SH. During JJA (Fig. 10b), this error becomes smaller with increasing resolution. In DJF (Fig. 10a), the error almost vanishes at T30 resolution and increases again, with the opposite sign, at higher resolution. The latter features, which arise through a mislocation of the westerly wind maxima located too far poleward in T42 and T106, are consistent with the zonally averaged sea level pressure and 500 hPa geopotential height shown in Figs. 1 and 4, respectively. The error patterns of the stationary wave part of the zonal wind are shown for the 850 hPa level (Fig. 11) and for the 250 hPa level (Fig. 12), respectively. As to be expected from the figures shown above (cf., Figs. 2b, 3b, 5 and 7), the error patterns are almost independent of resolution but the magnitudes (in terms of rmse) are becoming smaller with increasing resolution. Meridional profiles of zonally averaged low-level wind speed (at a height of 10 m) are shown in Fig. 13. At low latitudes, there is no clear resolution effect. Independent of resolution, the trade winds in the respective winter hemisphere are more vigorous than the ERA analyses. At mid-latitudes, the wind speed tends to increase with increasing resolution. However, compared to ERA, there is no clear improvement in the higher resolution models.

3.5 Precipitation

Fig. 14 shows meridional profiles of zonal averages of land and ocean precipitation for the different model resolutions as well as for ERA and observational analyses from GPCP. Here it has to be taken into account that the resolution of the GPCP data is relatively coarse (approximately

T42), so that it is unable to capture all details that are visible in the T106 simulation. Large differences between ERA and GPCP can be found in the tropics where ERA is known to be too wet (Stendel and Arpe, 1997). Here, the model simulations are generally between the ERA and GPCP estimates. There is no clear resolution dependence in the simulations except over the oceans where the tropical precipitation maxima are becoming more pronounced at higher resolution. Moreover, the double maximum of precipitation in DJF, with peaks at 10°S and 5°N, is captured better at higher resolution. In general, the agreement between the model simulations and ERA or GPCP, and also between these estimates themselves, is better in the NH than in the SH. Over the extratropical continents, differences in the zonal averages of precipitation are not systematic. Over the extratropical oceans, a general overestimation of precipitation in the respective winter hemisphere and an underestimation in the corresponding summer hemisphere can be found. These biases become more evident with increasing resolution.

From the global horizontal distributions shown in Fig. 15 it can be seen that local discrepancies between low and high resolution experiments can be quite large, the latter showing much more details related to orography. For example, with increasing resolution the tropical precipitation maximum in JJA concentrates more and more into a narrow band along the ITCZ with maxima over Central America, West Africa and Indonesia. In JJA, precipitation is overestimated over the tropical West Pacific, regardless of resolution, whereas in the equatorial East Pacific (near 120°W) considerably more rain falls in T106 than in the coarser resolution models which is in better agreement with GPCP estimates and also with ERA (not shown).

Over the western parts of the extratropical continents, which are frequently influenced by oceanic air masses, there is generally a slight underestimation of precipitation in the respective summer hemisphere, while in winter the opposite is true. This effect becomes larger with increasing resolution and can be seen clearly in the T106 simulation over Europe, as shown in Fig. 16. While in DJF the strongest westerlies are observed over the North Sea, this zone is shifted southward to Northern Germany and Poland in the T106 simulation, leading to anomalous advection of warm and moist oceanic air masses and therefore to a positive temperature bias and anomalously high precipitation. In JJA, on the other hand, there is an easterly wind bias (cf., Fig. 11b) which has the opposite effect, i.e., warming and drying of parts of Europe through anomalous advection of warm and dry air from the East. The warm and dry bias during JJA is most evident at T106 resolution (cf., Figs. 8b and 16b) and amplified through processes such as drying of the soil and reduced cloud cover.

The underestimation of the Indian summer monsoon in low-resolution simulations (i.e., coarser than T106) is a well-known problem of ECHAM4 (see R96 for a detailed discussion). To some extent, this is related to orography which is becoming more and more realistic with higher resolution (Fig. 17a). Obviously, the T106 model is able to simulate the precipitation pattern during the Indian summer monsoon, such as the maximum over the Western Ghats and the minimum in the lee of this mountain range, much better than the low-resolution models

(Fig. 17b). Although GPCP, due to its coarse resolution, is unable to capture all of the observed regional precipitation features over the Indian subcontinent, the T106 model is probably overestimating the precipitation along the coast of Burma and Thailand. On the other hand, there is still a deficit over India (although smaller than at T21, T30 and T42). As obvious from Fig. 17c, the low-resolution models are unable to correctly simulate the position and strength of the monsoon trough across North East India, and they also underestimate the low-level winds over the Bay of Bengal. The T106 model is able to capture these features very well.

3.6 Water vapour and clouds

The errors in vertically integrated specific humidity (or "total precipitable water", TPW) are shown in Fig. 18. Compared to ERA, the model tends to underestimate TPW in the subtropics where marine stratocumulus clouds prevail, i.e., off the west coasts of America and Africa. This dry bias, which is independent of resolution and season, is related to anomalous large-scale subsidence which tends to suppress the water abundance in these regions. On the other hand, in convectively active regions of the tropics such as the ITCZ and SPCZ, the TPW is overestimated by all of the models. As suggested by Chen et al. (1996), these low-latitude error patterns which are typical for ECHAM4 (i.e., a wet bias in wet areas and a dry bias in dry areas), are linked through overestimated tropical convection driving excessive tropical circulation systems such as the Hadley and Walker circulations. The wet bias over high northern latitudes during JJA is consistent with a warm bias in these regions (cf., Fig. 6b). As mentioned above, the Indian summer monsoon is underestimated in the low-resolution models but simulated acceptably at T106 resolution. This can also be analyzed from the TPW (Fig. 18b) which is underestimated at all resolutions except for T106 which simulates slightly higher TPW than ERA indicates.

These findings are consistent with the patterns of total cloud cover shown in Fig. 19. Compared to ISCCP (Rossow and Garder, 1993), there is a lack of marine stratocumulus off the west coasts of America and Africa. In general, the contrast between total cloud cover in convectively active regions in the tropics and the subtropical "desert" regions is larger in the models, especially at T106 resolution, than in the ISCCP data. Also the seasonal cycle over the NH continents is not very well simulated. While there is too much cloudiness in DJF, there is too little in JJA, especially at T106 resolution. Over the extratropical oceans, there is a cloud deficit throughout the year in both the SH and the NH, almost independent of resolution. These results are consistent with those obtained in a more detailed study by Chen and Roeckner (1997). Different from other studies (e.g., Kiehl and Williamson, 1991), there is little resolution dependence in the results. This applies not only for the global means but also, in general, for the regional distributions. Polar clouds have not been discussed in this study because the ISCCP data are unreliable at high latitudes.

3.7 Interim discussion

The simulation errors displayed in Figs. 1-19 are summarized in the following Tables, where RMS errors are shown separately for the zonal mean components (Table 3) and for the station-

Table 3: Root mean square (RMS) errors of **zonal mean** components in the ECHAM4 model with respect to the ECMWF reanalyses (ERA)

Quantity	Level [hPa]	Season	T21-ERA	T30-ERA	T42-ERA	T106-ERA
Sea level pressure [hPa]		DJF	5.44	2.18	2.10	2.29
		JJA	5.75	3.28	1.83	2.44
Geopotential [gpm]	850	DJF	46.5	15.1	17.5	20.8
		JJA	44.1	24.0	14.8	18.5
	500	DJF	68.5	32.2	38.4	49.6
		JJA	53.8	38.7	39.7	49.6
	250	DJF	76.7	61.0	74.0	103.6
		JJA	67.7	67.1	76.2	105.8
Temperature [K]	850	DJF	1.40	1.16	1.07	0.95
		JJA	1.69	2.21	2.12	2.20
	500	DJF	1.37	1.04	0.89	1.20
		JJA	1.38	1.10	0.93	1.21
	250	DJF	4.01	4.18	4.01	3.93
		JJA	3.37	3.39	3.32	3.44
Zonal wind [ms^{-1}]	850	DJF	2.56	0.63	1.26	1.71
		JJA	2.31	1.31	0.93	0.95
	500	DJF	4.34	1.59	1.80	2.15
		JJA	4.06	2.75	2.31	1.80
	250	DJF	6.10	3.14	2.54	2.86
		JJA	7.05	4.39	3.43	1.52
Mean rank			3.50	2.15	1.65	2.60

ary wave components (Table 4). The overall model performance is indicated by a "mean rank" which is obtained by assigning a rank for each variable, level and season shown in the respective Table (where '1' corresponds to the best performance and '4' to the worst) and finally taking the average of all ranks. As to be expected from the results shown in Figs. 1-19, the T21 model has the poorest ranks for both components. It is interesting to note that, for the zonal mean components, the medium resolution models (T30, T42) perform on average better than the T106 model. A degradation with increasing resolution is particularly evident for 250 hPa geopotential height (Table 3). On the other hand, the stationary wave components (Table 4) show a much more orderly behaviour, i.e., the T106 model has a mean rank of almost 1, and the other models follow with mean ranks close to the expected ones. In general, the error reductions with higher resolution are more pronounced in JJA than in DJF.

Table 4: Root mean square (RMS) errors of **stationary wave** components in the ECHAM4 model with respect to the ECMWF reanalyses (ERA)

Quantity	Level [hPa]	Season	T21-ERA	T30-ERA	T42-ERA	T106-ERA
Sea level pressure [hPa]		DJF	2.45	1.94	1.76	1.65
		JJA	2.78	2.35	1.87	1.18
Geopotential [gpm]	850	DJF	17.7	12.7	12.7	11.7
		JJA	20.4	17.5	14.3	9.4
	500	DJF	25.9	20.2	20.4	17.3
		JJA	23.7	21.3	19.5	12.7
	250	DJF	35.3	27.4	24.5	23.4
		JJA	40.7	36.7	32.3	18.6
Temperature [K]	850	DJF	1.34	1.23	1.16	1.03
		JJA	1.30	1.16	1.06	0.85
	500	DJF	0.98	0.82	0.63	0.61
		JJA	1.16	1.03	0.87	0.49
	250	DJF	0.80	0.80	0.74	0.78
		JJA	1.42	1.36	1.13	0.77
Zonal wind [ms^{-1}]	850	DJF	1.77	1.33	1.29	1.31
		JJA	1.94	1.68	1.53	1.27
	500	DJF	2.42	1.79	1.72	1.50
		JJA	2.34	2.05	1.93	1.52
	250	DJF	3.77	2.79	2.39	2.20
		JJA	4.37	3.58	2.10	1.78
Mean rank			3.95	2.85	2.00	1.10

The improvement in stationary-wave simulation at higher resolution may to some extent be caused by a better representation of orography at higher resolution. However, the improvement is more evident in the SH, where orographic forcing is small. Here, the phases of the stationary waves remain almost unchanged in the simulations while the amplitudes are gradually becoming reduced with higher resolution. Thus, it is essentially a gradual reduction in stationary-wave amplitudes which leads to the overall improvement at higher resolution.

The most puzzling aspect, however, is the deterioration of the zonal mean components in the T106 model. One region where the T106 model performs worse is the low-latitude upper troposphere where, for example, the warm temperature bias is clearly higher than in the other models (cf., Fig. 6a,b). Although this bias systematically increases from T21 to T106, the change is particularly evident from T42 to T106. One reason could be, for example, more efficient latent heat

uptake from the oceans by increased low-level wind speeds. However, as shown in Fig. 13, the 10m wind at low latitudes does hardly depend on resolution and the same applies for the latent heat flux over the oceans (not shown). Another process which could contribute to upper tropospheric heating is atmospheric trapping of longwave radiation by water vapour and clouds, especially high-level cirrus clouds. Actually, the total (i.e., cloud plus clear sky) greenhouse effect which can be defined as the difference between surface emission and outgoing longwave radiation (OLR) at the top of the atmosphere (Raval and Ramanathan, 1989), becomes largest, at low latitudes, in the T106 model. Consistent with the jump in the temperature bias, the largest jump in greenhouse effect (30 N to 30 S; mean of DJF and JJA) is found between T42 (200 Wm^{-2}) and T106 (205 Wm^{-2}). This additional greenhouse effect in the T106 model is particularly large in areas with deep convection. Some compensation, i.e., smaller values in the T106 model, are found in the subtropics as a result of reduced clouds and humidity due to enhanced subsidence.

According to Fig. 20 which shows the simulated distributions of cloud ice content at 250 hPa, there is ample evidence that the ice content in areas of deep convection is increasing with increasing resolution. The change is particularly evident from T42 to T106 resolution. More vigorous tropical convection in the T106 model is the primary source of increasing cloud ice which is then formed through detrainment at the level of vanishing buoyancy. The amount of cloud ice which stays at the detrainment level depends crucially on the fall velocity of ice crystals which is parameterized in terms of the cloud ice content (R96). Although the parameters in the cloud scheme have been adjusted to give a reasonable global mean radiation budget at all resolutions (cf., Table 2), this global adjustment does not account for regional compensation effects. For example, in tropical regions with deep convection, the T106 atmosphere is heated through enhanced cirrus clouds (compared to the other models). Since upper tropospheric temperature gradients are small at low latitudes, the extra heating is spread over the whole tropics and subtropics so that, particularly in cloud free areas, more longwave radiation can be emitted to space, due to higher temperatures, which compensates for the reduced OLR in regions with enhanced convection and cirrus anvils. In conclusion, the warm bias in the T106 model, compared to the other models, is probably the result of insufficient tuning of cirrus cloud lifetime (cf., Table 1).

4. Intraseasonal variability

The analysis of intraseasonal variability follows the standard procedure, where transient eddies are defined as departures of 12-hourly values of the respective variable from its seasonal mean. Transient variances and covariances are calculated from filtered time series of the respective season, subsequently averaged over that season and finally over the whole ensemble. Time filtering is performed according to Blackmon (1976) to separate high-frequency fluctuations associated with travelling cyclones and anticyclones from low-frequency fluctuations, which are

connected to blocking, decaying cyclones or transitions from one circulation regime to another. The former filter emphasized periods between about 2.5 and 6 days and will be referred to as "bandpass regime" in the remainder of the text. Periods between about 10 and 90 days are emphasized by the lowpass filter, and will be called "lowpass regime" henceforth. The seasonal cycle is removed from the lowpass filtered data according to the procedure described by Ponater et al. (1990). Stationary eddies are defined as departures from the respective zonal means when averaged over one season. This means that the variances and covariances of the stationary eddies are calculated for individual seasonal means and subsequently averaged over the complete ensemble. For both frequency bands, and for the stationary part as well, results will be shown as zonally averaged latitude-height cross sections. For the transient eddies, a few horizontal distributions are shown in addition. Results are presented for the T42 and T106 simulations of boreal winter (DJF). These model simulations are compared to both the operational ECMWF analyses, which have been widely used for model validation, and for the ECMWF reanalyses (ERA) which is considered as the most reliable observational estimate available.

4.1 Geopotential height variability

Fig. 21 shows latitude-height cross sections of transient variability (in terms of standard deviation) for both frequency bands (a,b) and for the stationary eddies (c) in addition. As already pointed out in the discussion of the jet core position, the model tends to shift the maxima of geopotential variability poleward and upward, especially in the SH. There is also a slight overestimation of the bandpass filtered maxima in both hemispheres. In the lowpass regime, reasonable agreement of model and ERA can be seen. In the NH, especially in the transition zone between the upper tropospheric jet and the polar night jet, geopotential variability is generally overestimated in the T106 simulation, whereas the agreement between T42 and ERA is better. For the stationary eddy variability, the differences are quite small. In T106, the NH maximum variability is overestimated by about 10% and displaced upward compared to ERA. Recent investigations (e.g. R96) pointed out that ECHAM4 underestimates the variability in the lowpass regime when compared to the operational ECMWF analyses. However, a comparison of model variabilities to those from operational analyses should be interpreted with caution. While differences between operational analyses and ERA are negligible in the bandpass regime, except near the polar night jet, the lowpass variability is artificially enhanced in the operational analyses by about 15%. This is due to the numerous changes that have been applied to both the ECMWF model layout and the data assimilation scheme in the course of the years (for a detailed description of these changes and their anticipated effects see Trenberth, 1992). In general, the notion that lowpass variability is systematically underestimated in ECHAM4 (R96) can no longer be maintained when ERA is used for validation instead of the operational analyses (see below).

Horizontal distributions of simulated and observed 1000 hPa geopotential height variability are presented in Fig. 22. In the bandpass regime (a), the model is able to capture the North Atlantic and North Pacific storm tracks as well as the SH circumpolar storm track quite well, with only minor differences between T42 and T106. An exception is the region between Scandinavia and

the Yenisey river, where variability is clearly underestimated in the T42 resolution run, as pointed out by R96, but captured reasonably well in the T106 simulation. On the other hand, an overestimation of variability in T106 can be found in the Icelandic region. Differences in the lowpass regime are more systematic (Fig. 22b). In T42, there is a general underestimation of variability over the East Atlantic and the western parts of Eurasia as well as in the entire extratropics of the SH. While the latter is captured better in the T106 simulation, geopotential variability is overestimated especially in the Arctic and in the Greenland Sea. At 500 hPa (Fig. 23), the T106 model overestimates the bandpass-filtered geopotential height variability (a) along the Atlantic storm track, over Europe and the western parts of Russia. In contrast, there is very good agreement along the Pacific storm track and in the SH. The T42 model, in the bandpass regime, is in slightly better agreement with ERA. A model deficit which has previously been analyzed for the T42 model (R96) is the too zonal orientation of the axis of maximum variability across the North Atlantic. This feature, which is even more pronounced in the T106 simulation, is consistent with the wind errors that were discussed above. For the lowpass regime (Fig. 23b), biases in the T106 run are relatively small except for a westward shift of maximum variability from the Baltic Sea to the British Isles. The T42 underestimates lowpass variability in the North Atlantic sector but captures the North Pacific maximum very well.

4.2 Eddy heat fluxes

Fig. 24 shows latitude-height cross sections of the zonally averaged meridional heat fluxes by transient (a,b) and stationary eddies (c). In the bandpass regime, the T106 model slightly overestimates the heat fluxes in the lower troposphere but there is good agreement between the simulations and ERA otherwise. In the lowpass regime (Fig. 24b), a downward displacement of the maxima of heat transport in the NH lower troposphere can be noticed (near 850 hPa in ERA, but 950 hPa in the model regardless of resolution). Furthermore, the maxima are overestimated by about 20%. There are some differences also in the SH, such as an equatorword shift and underestimation of the maxima in the lower troposphere and an upward shift of poleward heat flux from the upper troposphere in ERA to the lower stratosphere in the models. The poleward heat transports in the vicinity of the polar night jets are underestimated in both models, and are located too far north compared to ERA. The interhemispheric asymmetry in stationary heat fluxes (Fig. 24c) is captured very well by the models. By and large, there is little difference between analysed and simulated heat fluxes by stationary eddies, except for a slight overestimation and poleward displacement of the NH maxima in both models. The large heat fluxes near the coast of Antarctica are due to interpolation effects and should be disregarded. While differences in the bandpass regime are minor, horizontal distributions of the lowpass meridional heat flux at 850 hPa (not shown) suggest that ECHAM4 overestimates the number and/or intensity of blocking-type flow patterns in the North Pacific. Such events are typically connected with large heat fluxes in the lowpass regime, and the fluxes over the Bering Sea are actually overestimated by 30% in T106 and by 60% in T42.

4.3 Eddy momentum fluxes

Latitude-height cross sections of the zonally averaged meridional momentum transport are shown in Fig. 25. In the bandpass regime (a), there is little difference between the model simulations and ERA, except for the notorious upward displacement of the maxima and a poleward shift in the SH. Furthermore, the SH momentum fluxes are slightly overestimated, which agrees with R96's findings. In the lowpass regime (b), fluxes are slightly underestimated in the SH, but overestimated in the NH, especially in the T106 simulation. It should be pointed out that operational analyses and ERA differ considerably in the lowpass regime, in particular in the NH. As discussed by Stendel and Arpe (1997, see their Fig. 1), this is due to the fact that there was almost no Hadley circulation in the operational analyses prior to 1982, when the nonlinear Normal Mode initialization was introduced. The Hadley cell remained much too weak until 1985, when the T106 model was introduced and substantial changes were applied to the parameterization of clouds, convection and condensation (see e.g. the discussion by Trenberth, 1992). Momentum fluxes by stationary eddies are captured very well in the simulations. While differences between the models are small in the vicinity of the NH subtropical jet and for the upper equatorial westerly winds, the T106 simulation is superior concerning the southward momentum transport near 60°N. Fluxes in the SH are negligibly small in both models and ERA.

4.4 Eddy kinetic energy

Cross sections of the zonal mean eddy kinetic energy of transient and stationary eddies are presented in Fig. 26. In the bandpass regime (a), the T106 model has slightly higher values than T42. In the NH, the latter fits to ERA very well while the opposite is true for the SH. However, the difference between the models and ERA are reasonably small and possibly within the range of observational uncertainty. In the lowpass regime (b) the T106 values exceed those of T42. Compared to ERA, the T42 values are too small in both hemispheres while the T106 values are somewhat on the high side in the NH, and somewhat on the low side in the SH. Similar to the momentum fluxes (c.f., Fig. 26b), there are large differences between operational analyses and ERA, the former exceeding ERA by up to 40%. Similar to the transient eddies, the kinetic energy of stationary eddies (Fig. 26c) is slightly increasing with increasing resolution and is, in general, somewhat higher than in ERA, except in the region of the polar night jet.

5. Concluding remarks

In this study we have compared the time-mean climate and its intraseasonal variability simulated by the MPI ECHAM4 model at four different horizontal resolutions, T21, T30, T42 and T106. For the purpose of model validation we have used chiefly ECMWF reanalyses (ERA). As

indicated in the Introduction, the main questions that have been addressed are (i) is there a systematic change of the simulated climate statistics with changing resolution, and (ii) to what extent does increasing resolution improve the simulated climate statistics?

To answer the latter question first, the most systematic improvement with resolution has been found for the zonally asymmetric, or stationary wave, components although this does not apply for every regional detail. Apart from a general reduction of truncation errors, the improvement in stationary wave patterns is probably related to a better representation of orography in the higher resolution models. While this may apply to the Northern Hemisphere, the error reduction in the Southern Hemisphere is caused by a gradual reduction of the zonally asymmetric components of wind, temperature etc. with increasing resolution. In general, a more realistic orography helps to improve the simulation of near-surface air temperature and precipitation. One example is the Indian summer monsoon which all of the models underestimate except for the T106 model which is able to capture not only the observed precipitation distribution but also the low-level wind patterns.

A systematic resolution dependence can be found for zonal mean sea level pressure, for example. Here, an improved simulation with increasing resolution is more obvious for JJA than for DJF. A distinct resolution dependence is found for the SH where the main pressure systems such as the subtropical high and the subpolar trough around Antarctica become more pronounced with higher resolution while their position is gradually moving poleward. A similar behaviour, in both hemispheres and independent of season, can be seen for the zonal mean geopotential height at 500 hPa. This indicates a deep-layer warming and poleward expansion of the warm tropics and subtropics which is obvious also in the low-latitude warm temperature biases which increase substantially from T42 to T106 resolution. This increasingly warm bias is caused by enhanced trapping of longwave radiation in the tropical atmosphere due to abundant cirrus clouds in the T106 model. The deterioration of the zonally symmetric components in the T106 model can partly be attributed to insufficient tuning of the cloud model.

The resolution dependence of the simulated intraseasonal variability has only been estimated for the higher resolution models, T42 and T106. Compared to ERA, both models are able to simulate reasonably well the intraseasonal geopotential height variability, eddy fluxes of heat and momentum, and eddy kinetic energy. This applies to transient eddies in both the bandpass and lowpass regime and to the stationary eddy variances and covariances as well. With respect to all of these components, the T106 model yields somewhat higher values than the T42 model. In general, the T106 values, compared to ERA, are somewhat on the high side while the T42 values tend to be on the low side. Regionally, the resolution dependence is larger in the North Atlantic/Europe region than in the North Pacific. For example, the biases in sea level pressure and geopotential height in DJF imply an unrealistic zonalisation of the wind over Europe, increasing with increasing resolution, whereas the flow across the North Pacific is simulated reasonably well at all resolutions.

Some biases can be identified which are more or less independent of resolution and may therefore be attributed to deficiencies in the physical parameterizations. Among these are the overestimation of the intensity and the mislocation of the Azores high, a cold bias in the polar upper troposphere and lower stratosphere (especially over the respective summer pole) as well as the poleward and upward displacement of the maxima of most variables, in particular in the Southern Hemisphere.

Large differences exist between the eddy statistics of the ECMWF operational analyses and ERA, especially for the wind-field related quantities (i.e., momentum transport and kinetic energy of transient eddies). As a result of numerous changes that have been applied to the operational model, the lowpass variability in the operational analyses is significantly higher than in ERA. Differences in the bandpass regime and for the stationary eddies are smaller. This implies that our results are not directly comparable to previous investigations that used operational analyses for validation.

We infer from this study that increased horizontal resolution will not automatically reduce the systematic model errors because some of the physical parameterizations are resolution dependent and have been optimized, in general, at lower horizontal resolution. While this applies to large-scale climate statistics, a more direct, and positive, impact can be expected for the simulation of smaller-scale individual processes such as tropical cyclones, for example, which are well captured at T106 resolution (Bengtsson et al., 1995) but can hardly be resolved at a resolution of T42 or coarser.

Acknowledgments

We are indebted to our colleagues at the Max-Planck-Institut für Meteorologie in Hamburg, in particular Klaus Arpe and Michael Christoph, and at the German Climate Computing Centre for constructive discussions and generous technical assistance and to the ECMWF where the high resolution simulation was carried out. Helpful comments from Ulrike Lohmann are also acknowlegded. This study was supported by the EU project "High resolution 10 year climate simulation" (HIRETYCS), contract number **ENV-CT95-0184**.

References

Bengtsson, L., M. Botzet and M. Esch, 1995: Hurricane-type vortices in a general circulation model. *Tellus* **47A**, 175-196.

Blackmon, M.L., 1976: A climatological spectral study of the 500 mb geopotential height of the Northern Hemisphere. *J. Atm. Sci.* **33**, 1607-1623.

Boer, G.J., K. Arpe, M. Blackmon, M. Déqué, W.L. Gates, T.L. Hart, H. LeTreut, E. Roeckner, D.A. Sheinin, I. Simmonds, R.N.B. Smith, T. Tokiota, R.T. Wetherald and D. Williamson, 1992: Some results from an intercomparison of the climates simulated by 14 atmospheric general circulation models. *J. Geoph. Res.* **97**, 12771-12786.

Boer, G.J. and M. Lazare, 1988: Some results concerning the effect of horizontal resolution and gravity wave drag on simulated climate. *J. Clim.* **1**, 789-806.

Boville, B.A., 1991: Sensitivity of simulated climate to model resolution. *J. Clim.* **4**, 469-485.

Boyle, J.S., 1993: Sensitivity of dynamical quantities to horizontal resolution for a climate simulation using the ECMWF (cycle 33) model. *J. Clim.* **6**, 796-815.

Brinkop, S. and E. Roeckner, 1995: Sensitivity of a general circulation model to parameterizations of cloud-turbulence interactions in the atmospheric boundary layer. *Tellus* **47A**, 197-220.

Chen, C.-T., E. Roeckner and B.J. Soden, 1996: A comparison of satellite observations and model simulations of column-integrated moisture and upper-tropospheric humidity. *J. Clim.* **9**, 1561-1585.

Chen, C.-T. and E. Roeckner, 1997: Cloud simulations with the Max Planck Institute for Meteorology general circulation model ECHAM4 and comparison with observations. *J. Geophys. Res.* **102**, 9335-9350.

Claussen, M., U. Lohmann, E. Roeckner and U. Schulzweida, 1994: A global data set of land-surface parameters. *Max-Planck-Institut für Meteorologie* Report No. **135**, 34 pp.

Déqué, M., C. Dreverton, A. Braun and D. Cariolle, 1994: The ARPEGE/IFS atmosphere model: A contribution to the French community climate modelling. *Clim. Dyn.* **10**, 249-266.

Déqué, M. and J. P. Piedelievre, 1995: High resolution climate simulation over Europe. *Clim. Dyn.* **11**, 321-339.

Fouquart, Y. and B. Bonnel, 1980: Computations of solar heating of the Earth's atmosphere: A new parameterization. *Beitr. Phys. Atmos.* **53**, 35-62.

Gates, W.L., 1992: AMIP: The atmospheric model intercomparison project. *Bull. Am. Met. Soc.* **73**, 1962-1970.

Gibson, J. K., P. Kallberg, S. Uppala, A. Hernandez, A. Nomura and E. Serrano, 1997: ECMWF Re-Analysis Project Report, 1. ERA description. European Centre for Medium-Range Weather Forecasts, Reading, UK.

Giorgetta, M. and M. Wild, 1995: The water vapour continuum and its representation in ECHAM4. *Max-Planck-Institut für Meteorologie* Report No. **162**, 38 pp.

Hartmann, D., 1993: Radiative effects of clouds on Earth's climate. In: *Aerosol-Cloud-Climate Interactions*, ed. P.V. Hobbs, 151-173, Academic Press.

Huffman, G.J., R.F. Adler, B. Rudolf, U. Schneider and P.R. Keehn, 1995: Global precipitation estimates based on a technique for combining satellite-based estimates, rain gauge analysis, and NMP model precipitation information. *J. Clim.* **8**, 1284-1295.

Kiehl, J.T. and D.L. Williamson, Dependence of cloud amount on horizontal resolution in the National Center for Atmospheric Research community climate model. *J. Geoph. Res.* **96**, 10955-10980.

Louis, J.F., 1979: A parametric model of vertical eddy fluxes in the atmosphere. *Bound. Layer Meteor.* **17**, 187-202.

Mahlman, J.D. and L.J. Umbscheid, 1987: Comprehensive modeling of the middle atmosphere: the influence of resolution. In: *Transport processes in the middle atmosphere*, G. Visconti and R. Garcia (eds.), D. Reidel, 251-266.

McFarlane, N.A., 1987: The effect of orographically excited gravity-wave drag on the general circulation of the lower stratosphere and troposphere. *J. Atm. Sci.* **44**, 1775-1800.

Miller, M.J., T.N. Palmer and R. Swinbank, 1989: Parameterization and influence of sub-grid scale orography in general circulation and numerical weather prediction models. *Met. Atm. Phys.* **40**, 84-109.

Morcrette, J.-J., L. Smith and Y. Fouquart, 1986: Pressure and temperature dependence of the absorption in longwave radiation parameterizations. *Beitr. Phys. Atmos.* **59**, 455-469.

Nordeng, T.E., 1994: Extended versions of the convective parameterization scheme at ECMWF and their impact on the mean and transient activity of the model in the tropics. ECMWF Research Department,Technical Memorandum No. 206, October 1994, 41 pp., European Centre for Medium Range Weather Forecasts, Reading, UK.

Olson, J.S., J.A. Watts and L.J. Allison, 1983: Carbon in live vegetation of major world ecosystems. **ORNL-5682**, Oak Ridge Laboratory, Oak Ridge, Tennessee, USA.

Palmer, T.N., G.J. Shutts and R. Swinbank, 1986: Alleviation of a systematic westerly bias in general circulation and numerical weather prediction models through an orographic gravity wave drag parameterization. *Quart. J. Roy. Met. Soc.* **112**, 1001-1031.

Ponater, M., E. Kirk and U. Schlese, 1990: GCM-simulated transient variability in the Northern Hemisphere extratropics and its sensitivity to sea surface temperature variation. *Beitr. Phys. Atmosph.* **63**, 189-204.

Raval, A. and V. Ramanathan, 1989: Observational determination of the greenhouse effect. *Nature* **342**, 758-761.

Reynolds, R.W., 1988: A real-time global sea surface temperature analysis. *J. Clim.* **1**, 75-86.

Rockel, B. E. Raschke and B. Weyres, 1991: A parameterization of broad band radiative transfer properties of water, ice and mixed clouds. *Beitr. Phys. Atm.* **64**, 1-12.

Roeckner, E., K. Arpe, L. Bengtsson, S. Brinkop, L. Dümenil, M. Esch, E. Kirk, F. Lunkeit, M. Ponater, B. Rockel, R. Sausen, U. Schlese, S. Schubert and M. Windelband, 1992: Simulation of the present-day climate with the ECHAM model: Impact of model physics and resolution. *Max-Planck-Institut für Meteorologie* Report No. **93**, 171 pp.

Roeckner, E., 1995: Parameterization of cloud radiative properties in the ECHAM4 model. In: *Proceedings of the WCRP Workshop on „Cloud Microphysics Parameterizations in Global Atmospheric Circulation Models"*, May 23-25, 1995, Kananaskis, Alberta, Canada, WCRP Report No. **90**, 105-116, WMO-TD-No. 713.

Roeckner, E., K. Arpe, L. Bengtsson, M. Christoph, M. Claussen, L. Dümenil, M. Esch, M. Giorgetta, U. Schlese and U. Schulzweida, 1996: The atmospheric general circulation model ECHAM-4: Model description and simulation of present-day climate. *Max-Planck-Institut für Meteorologie* Report No. **218**, 90 pp.

Rossow, W.B. and L.C. Garder, 1993: Validation of ISCCP cloud detections. *J. Clim.* **6**, 2370-2393

Stendel, M. and K. Arpe, 1997: Evaluation of the hydrological cycle in reanalyses and observations. *Max-Planck-Institut für Meteorologie* Report No. **228**, 52 pp.

Tiedtke, M., 1989: A comprehensive mass flux scheme for cumulus parameterization in large-scale models. *Mon. Wea. Rev.* **117**, 1779-1800.

Trenberth, K.E., 1992: Global analyses from ECMWF and atlas of 1000 to 10 mb circulation statistics. *NCAR Technical Note* NCAR/TN-**373**+STR, 191 pp.+24 fiches.

Williamson, D.L. and P.J. Rasch, 1994: Water vapor transport in the NCAR CCM2. *Tellus* **46A**, 34-51.

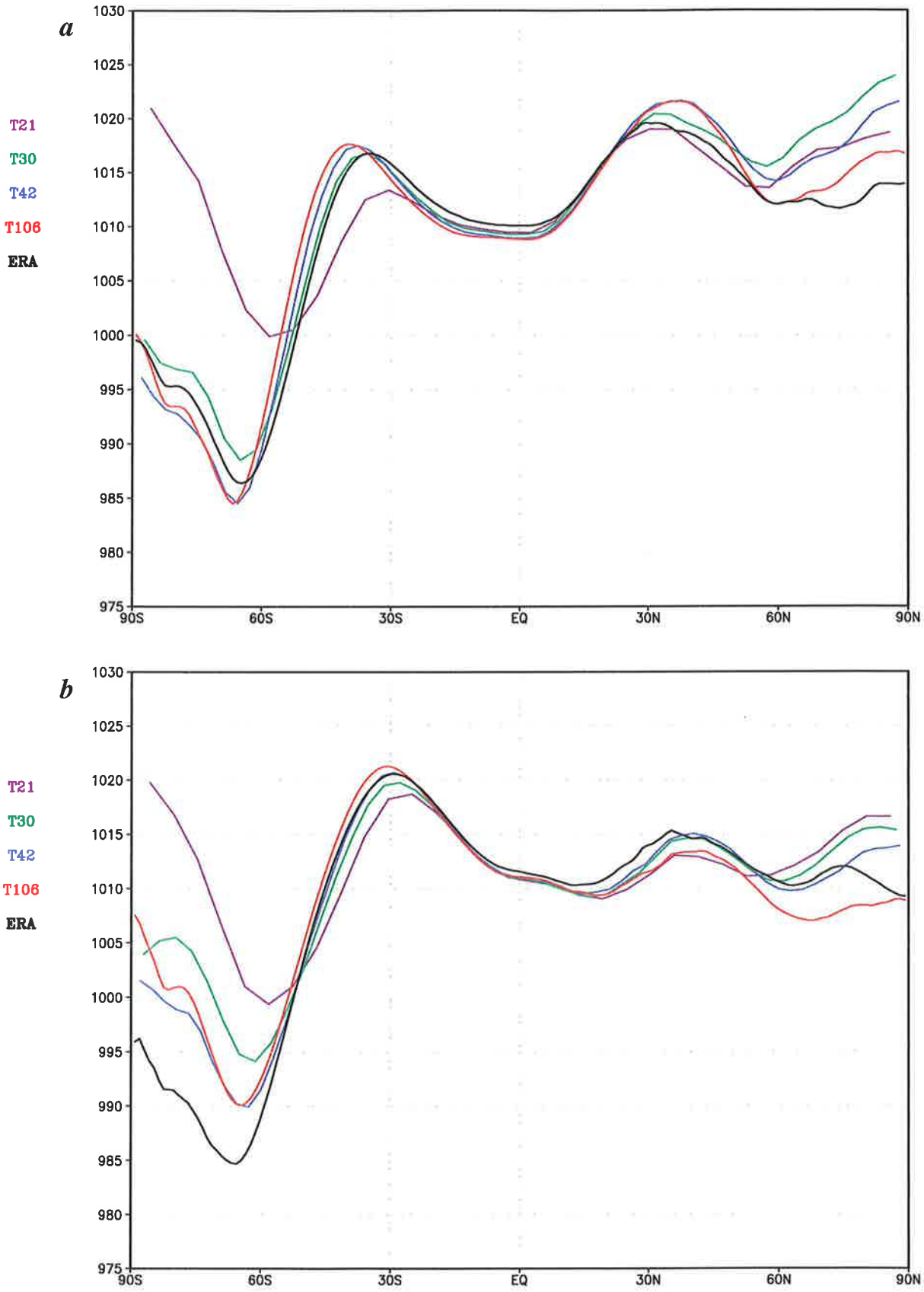

Fig. 1: Zonal mean sea level pressure for model resolutions T21, T30, T42, T106 and for the ECMWF reanalysis (a) for boreal winter (DJF) and (b) for boreal summer (JJA).

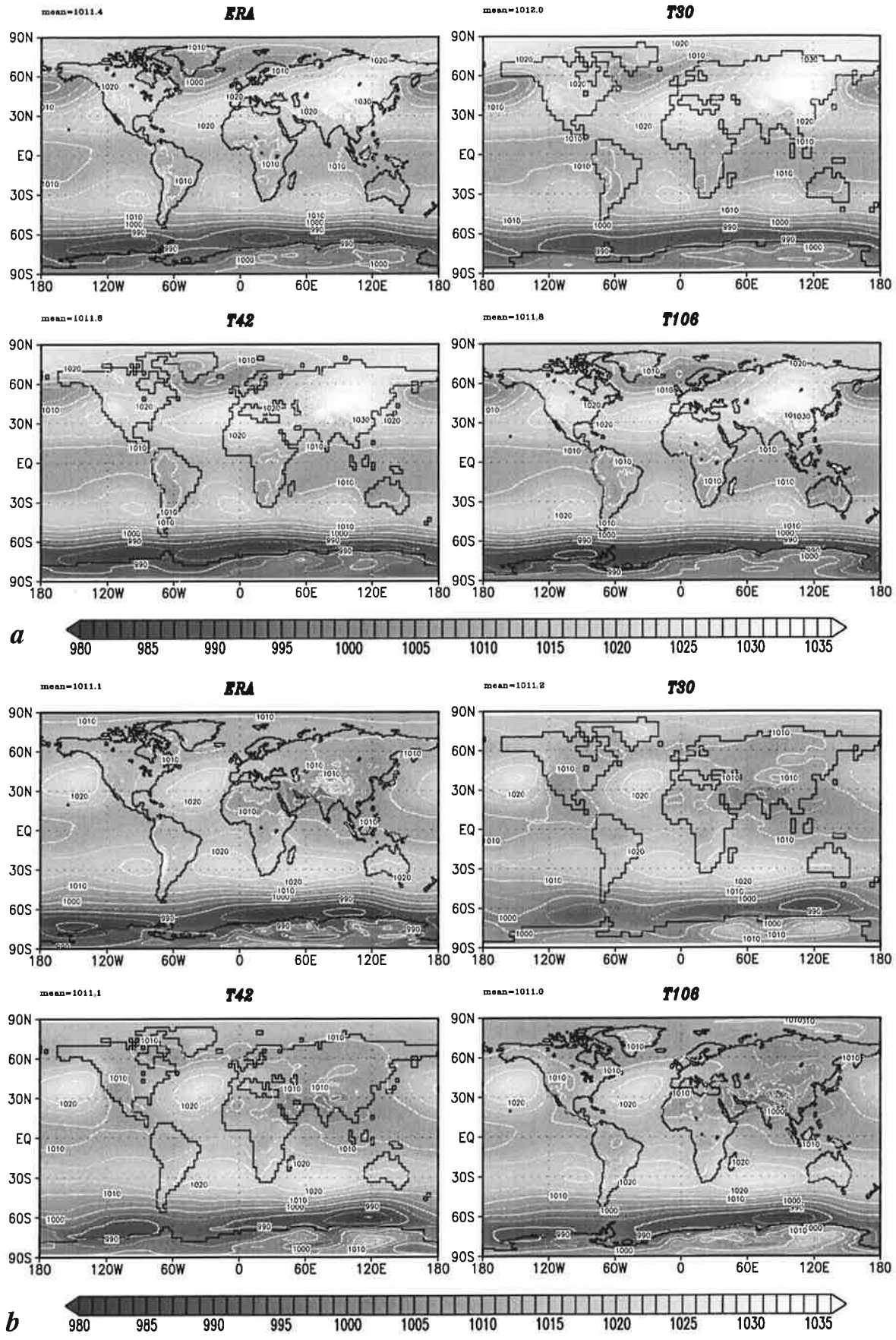

Fig. 2: (a) Mean sea level pressure for ERA and for different ECHAM4 resolutions (a) in boreal winter (DJF) and (b) in boreal summer (JJA). Contour interval 5 hPa.

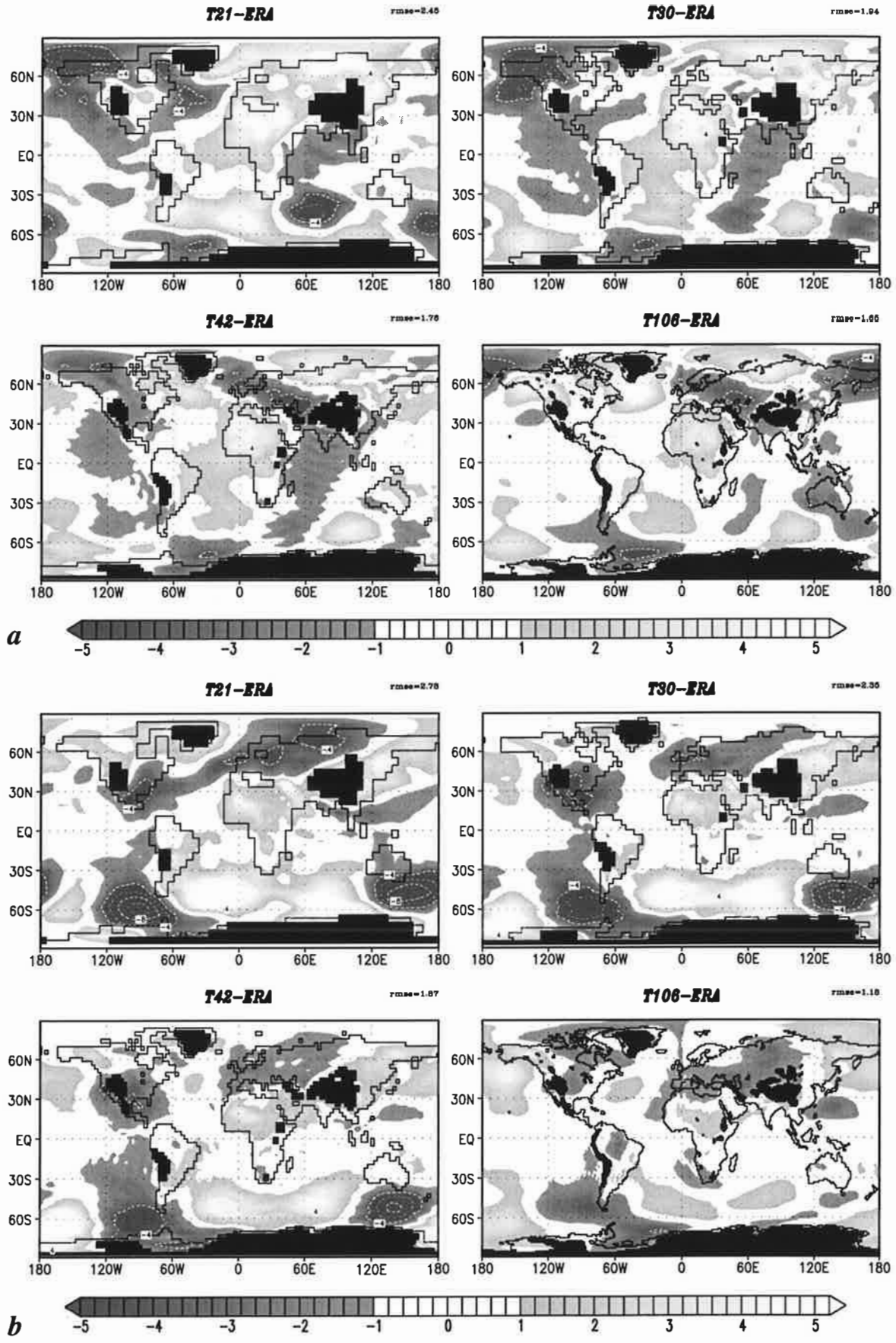

Fig. 3: Mean sea level pressure errors (a) in boreal winter (DJF) and (b) in boreal summer (JJA). Zonal mean removed, contour interval 2 hPa, zero line omitted. Terrain > 1500 m blanked out.

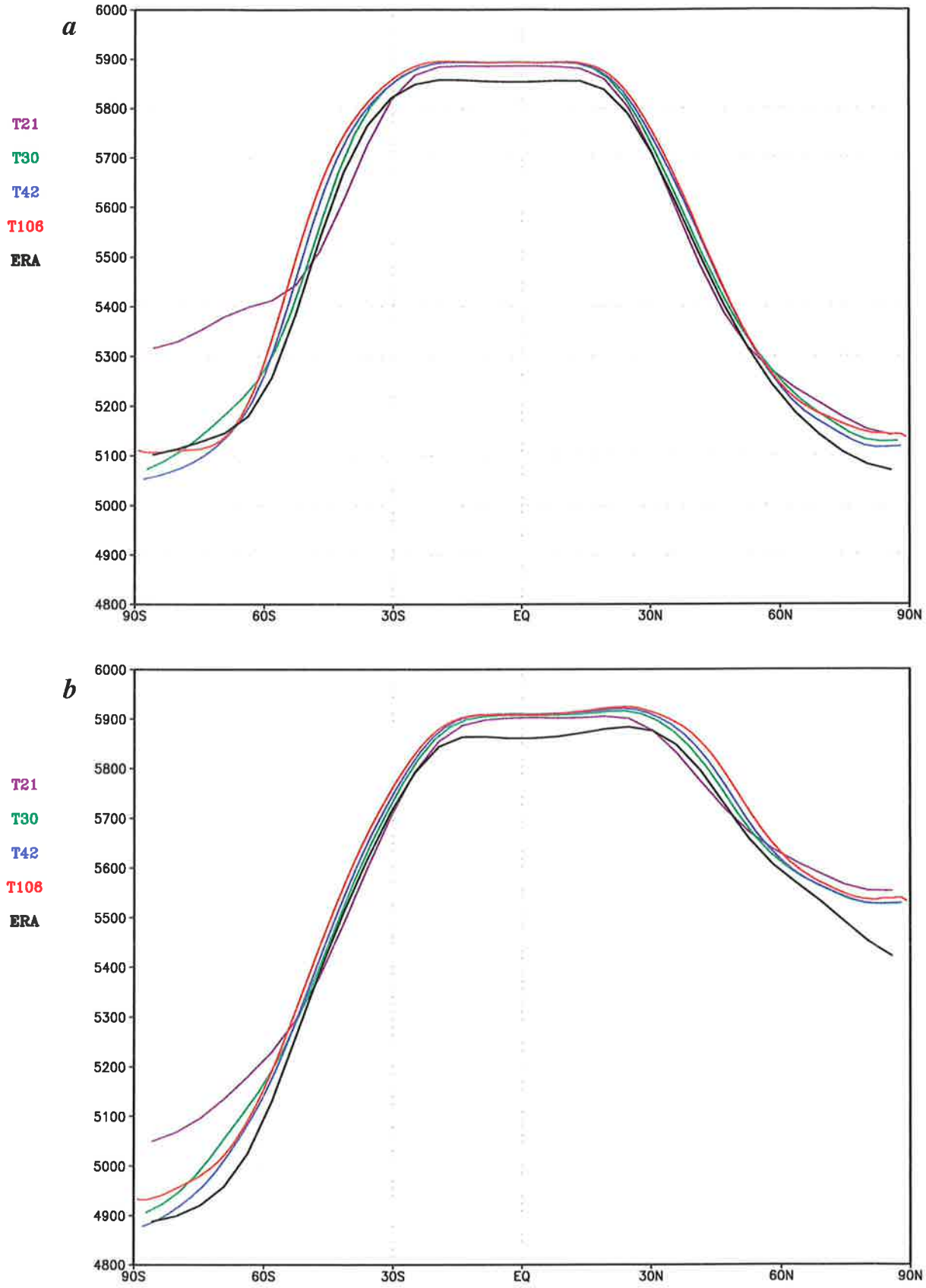

Fig. 4: As Fig. 1, for 500 hPa geopotential.

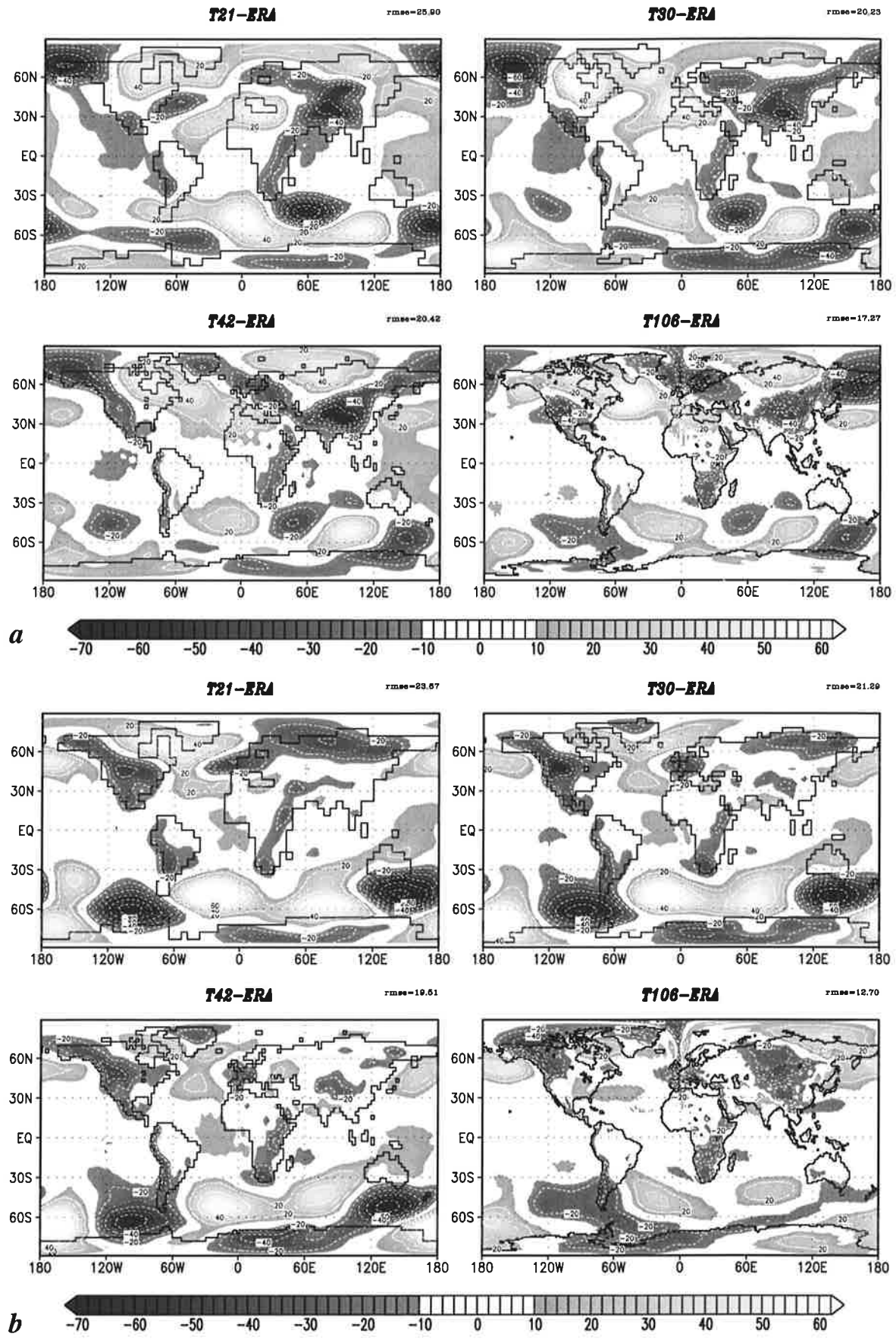

Fig. 5: 500 hPa geopotential height errors for different ECHAM4 resolutions (a) in boreal winter (DJF) and (b) in boreal summer (JJA). Zonal mean removed, contour interval 10 gpm.

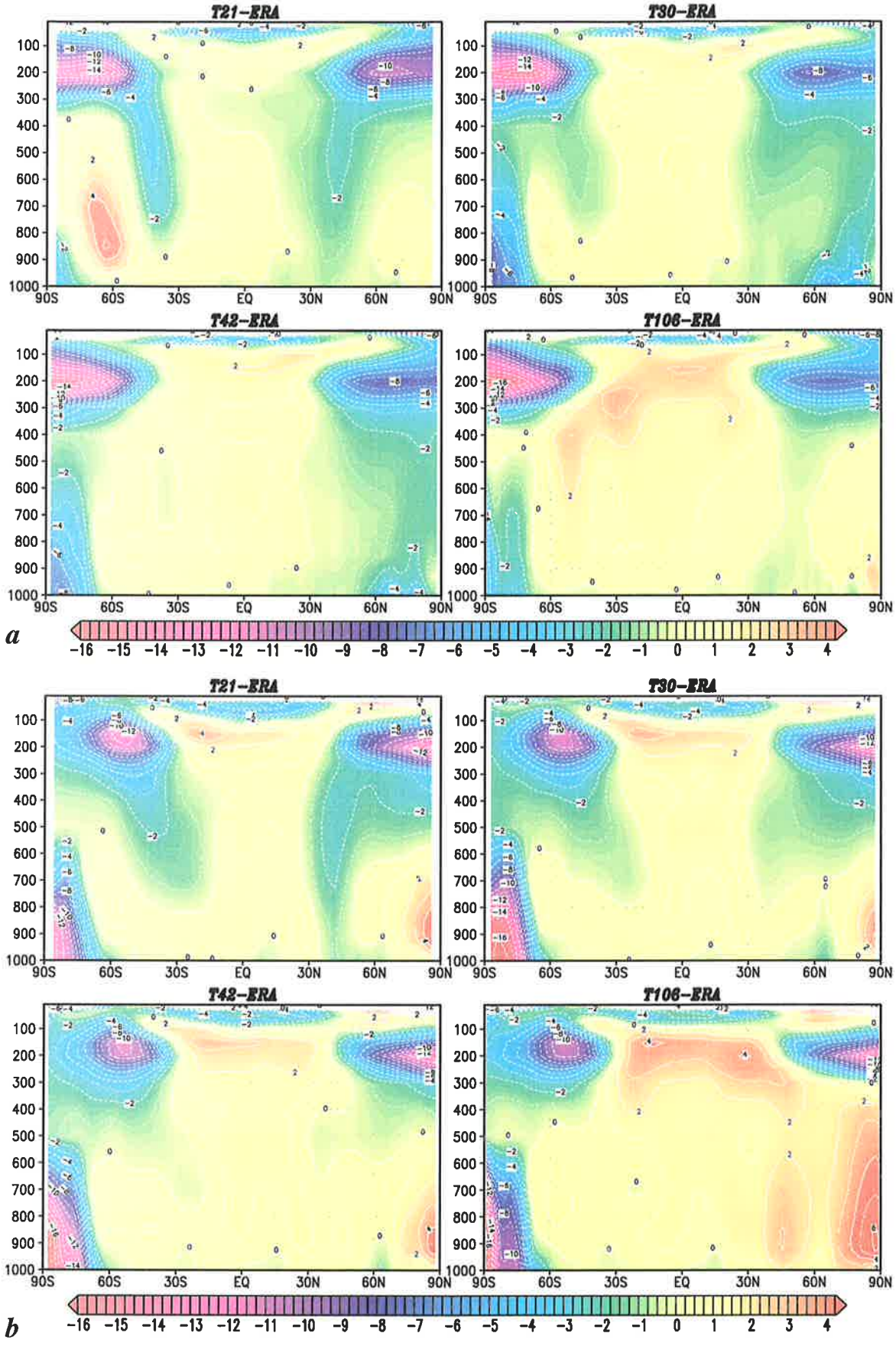

Fig. 6: Latitude-pressure cross sections of the temperature errors for different ECHAM4 resolutions (a) in boreal winter (DJF) and (b) in boreal summer (JJA). Contour interval 2 K.

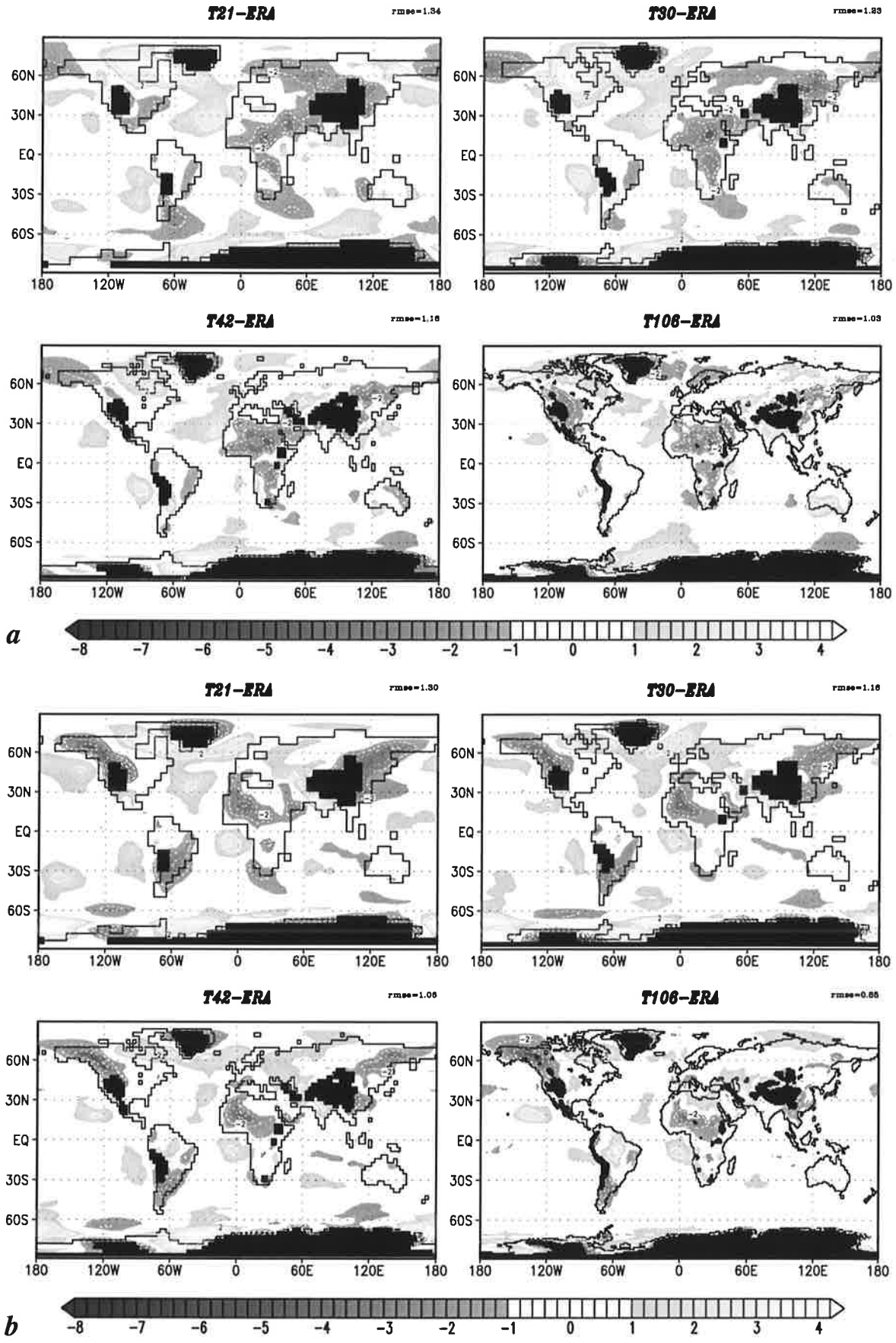

Fig. 7: As Fig. 5, for 850 hPa temperature. Terrain above 1500 m blanked out. Contour interval 2 K.

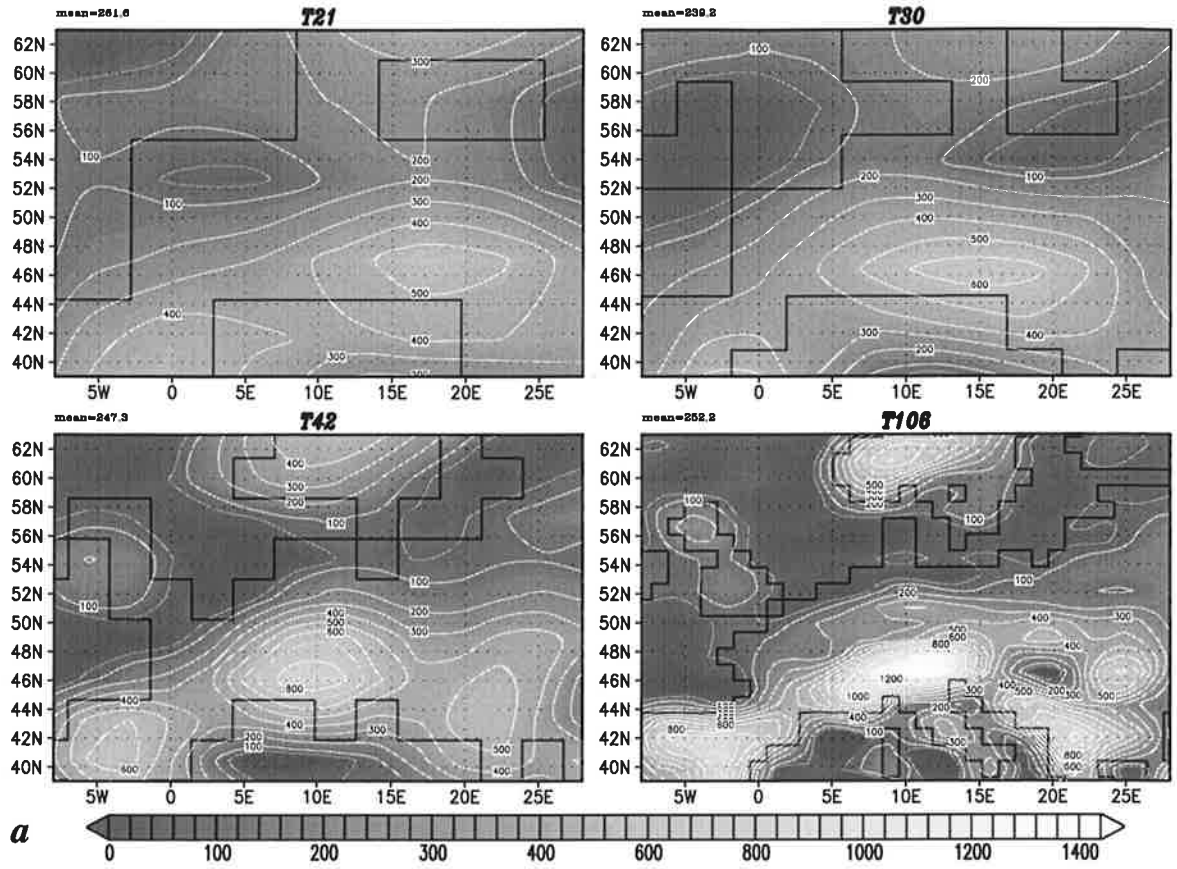

Fig. 8: (a) Orography over Europe for different ECHAM4 resolutions. Contours at 50, 100, 200, 300, 400, 500, 600, 700, 800, 900, 1000, 1200 and 1400 m. (b) Boreal winter (DJF) and (c) boreal summer (JJA) 2 m temperature over Europe for ERA and for different ECHAM4 resolutions. Contour interval 1 K.

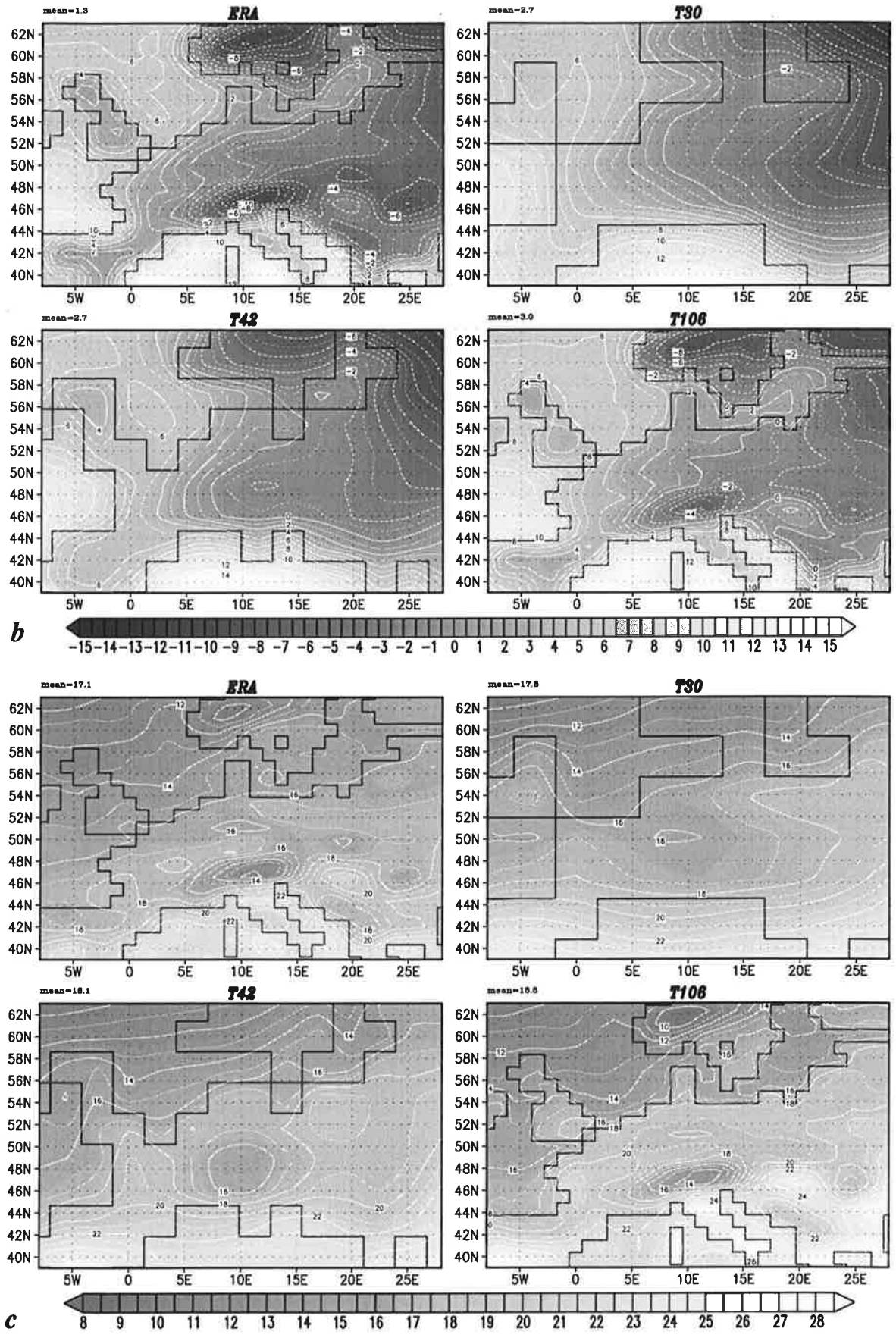
mean=1.3
ERA
mean=2.7
T30
mean=2.7
T42
mean=3.0
T106
62N
60N
58N
56N
54N
52N
50N
48N
46N
44N
42N
40N
5W
0
5E
10E
15E
20E
25E
b
-15 -14 -13 -12 -11 -10 -9 -8 -7 -6 -5 -4 -3 -2 -1 0 1 2 3 4 5 6 7 8 9 10 11 12 13 14 15
mean=17.1
ERA
mean=17.6
T30
mean=16.1
T42
mean=16.6
T106
c
8 9 10 11 12 13 14 15 16 17 18 19 20 21 22 23 24 25 26 27 28

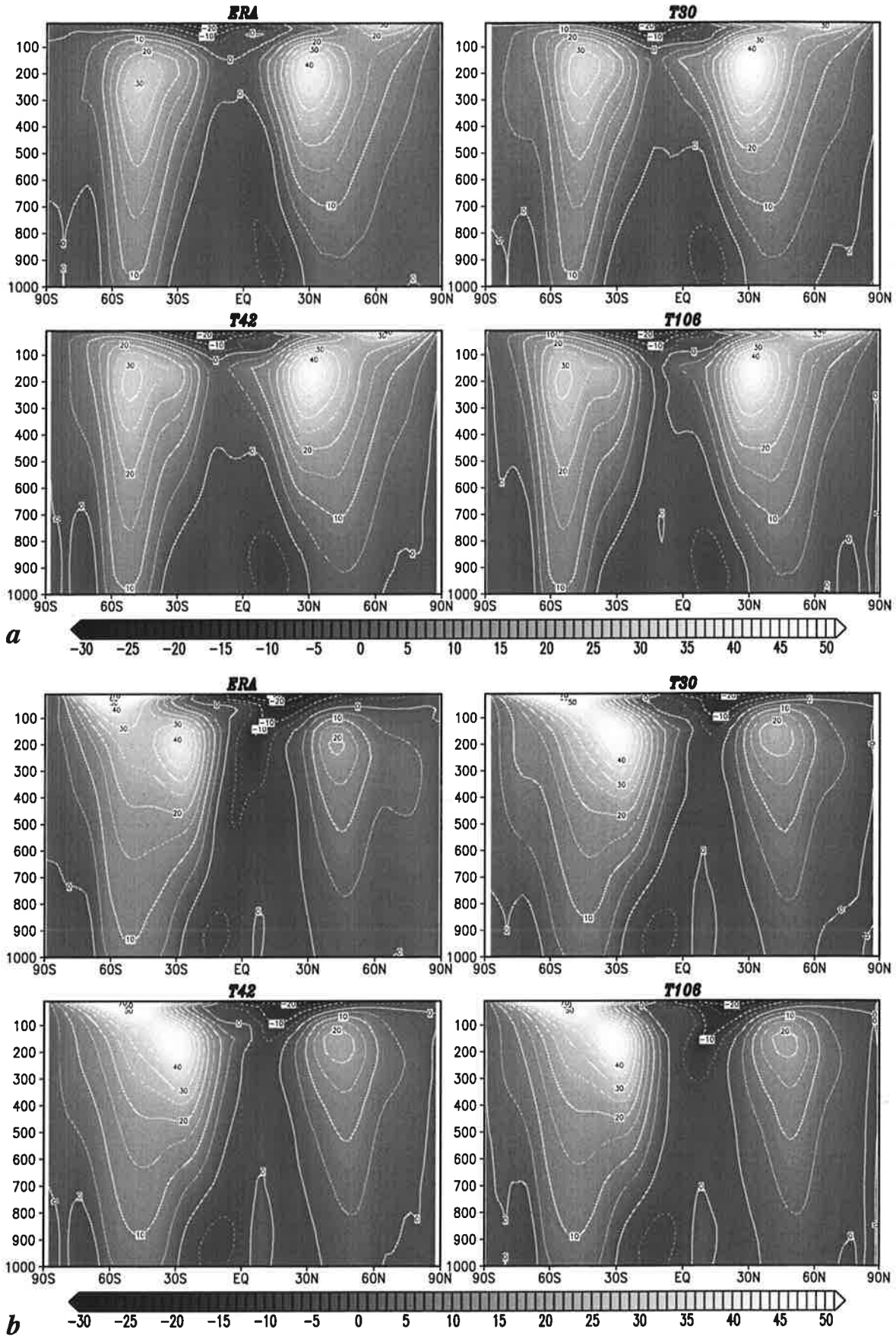

Fig. 9: Latitude-pressure cross sections of the zonal wind component for ERA and for different ECHAM4 resolutions (a) in boreal winter (DJF) and (b) in boreal summer (JJA). Contour interval 5 ms^{-1}.

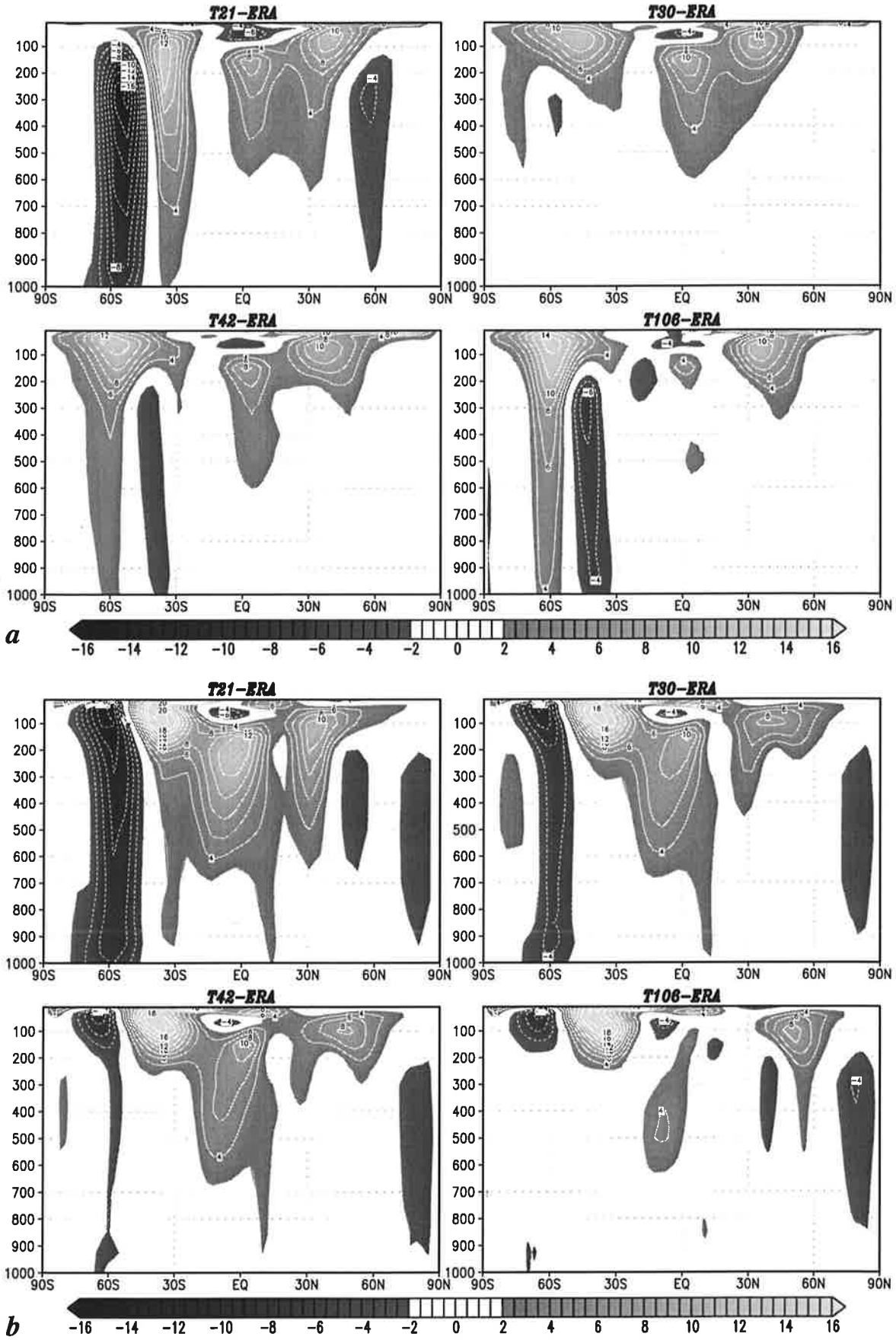

Fig. 10: Latitude-pressure cross sections of the zonal wind error for different ECHAM4 resolutions (a) in boreal winter (DJF) and (b) in boreal summer (JJA). Contour interval 2 ms^{-1}.

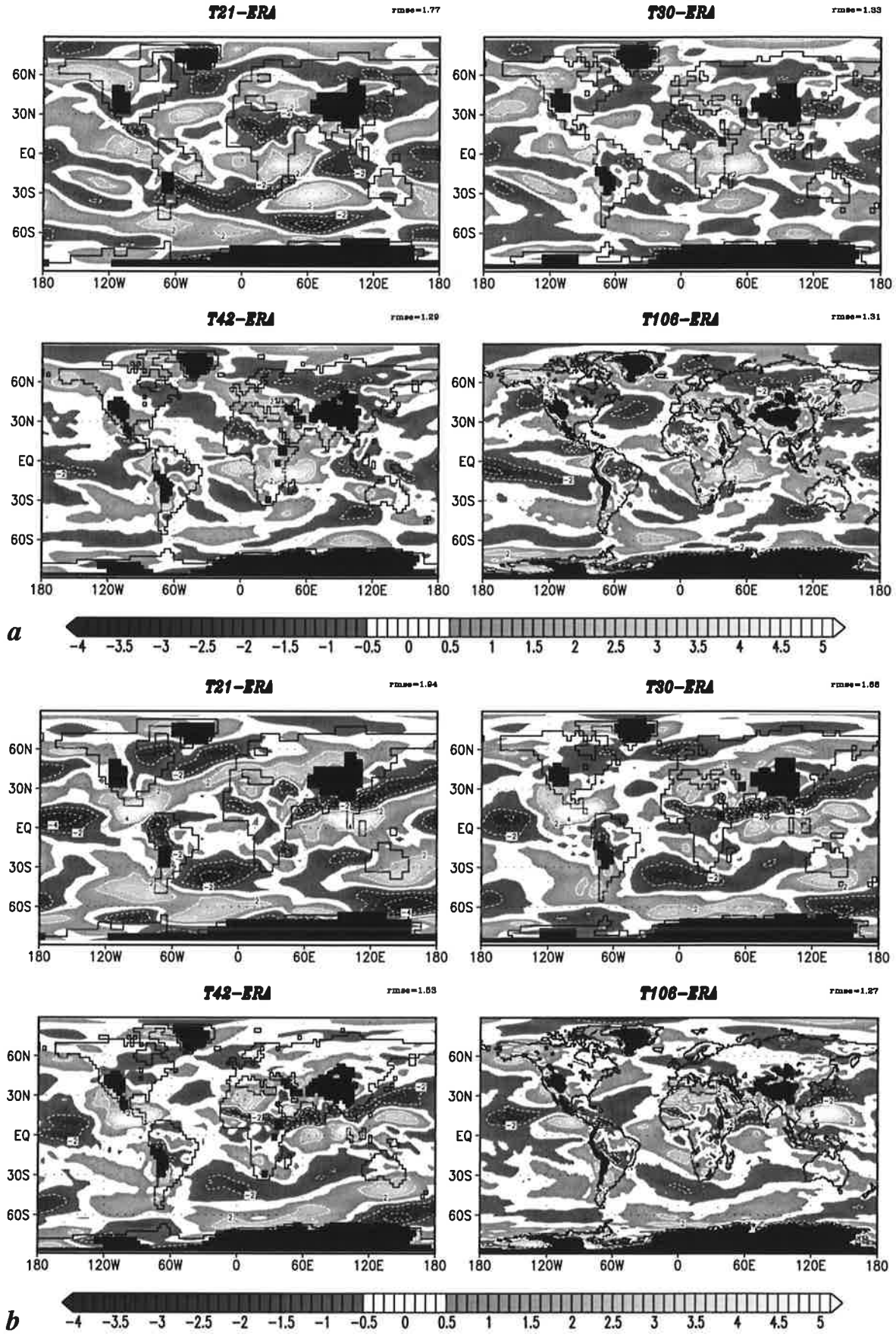

Fig. 11: 850 hPa zonal wind errors for different ECHAM4 resolutions (a) in boreal winter (DJF) and (b) in boreal summer (JJA). Zonal mean removed, terrain above 1500 m blanked out. Contour interval 2 ms^{-1}.

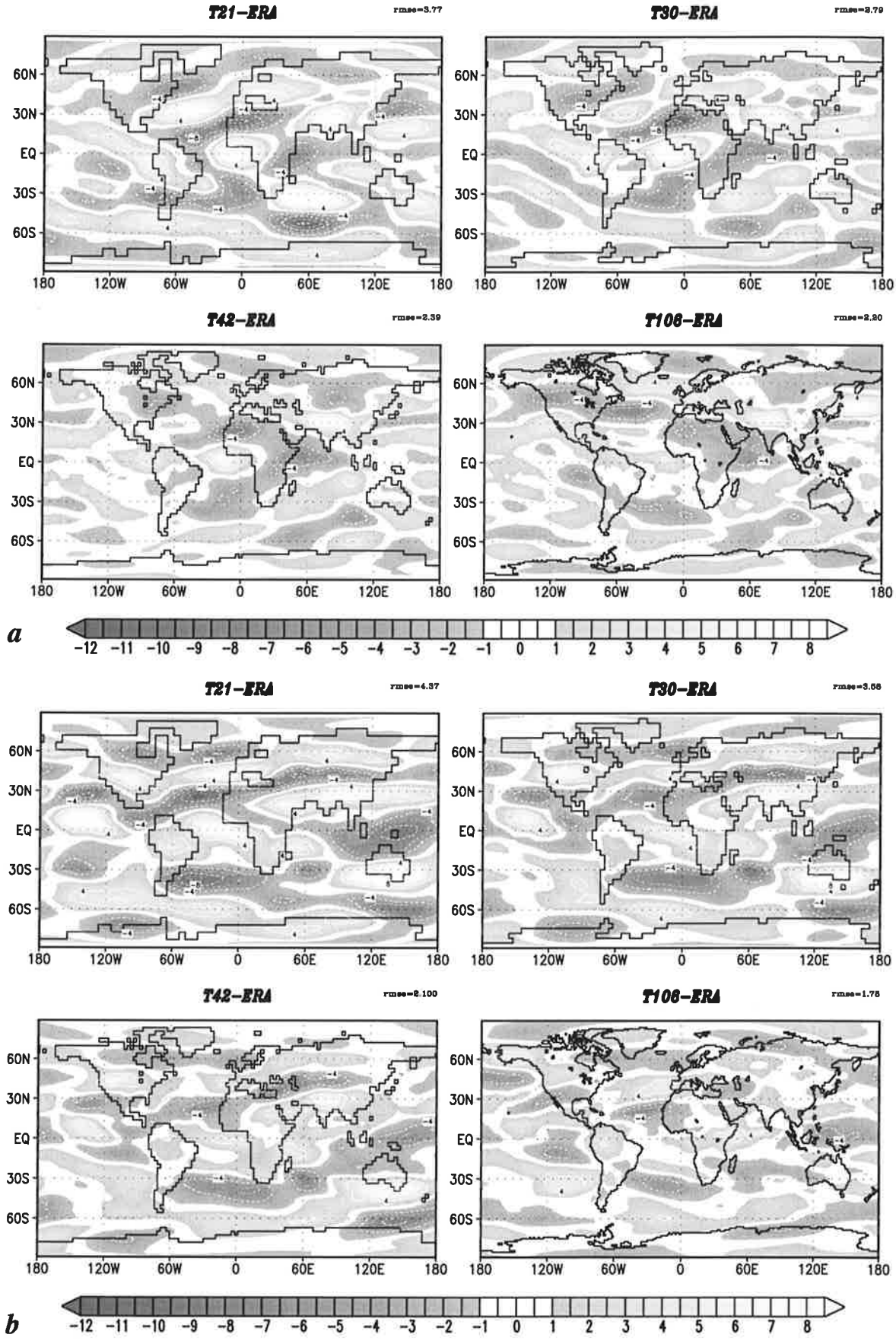

Fig. 12: As Fig. 11, for 250 hPa.

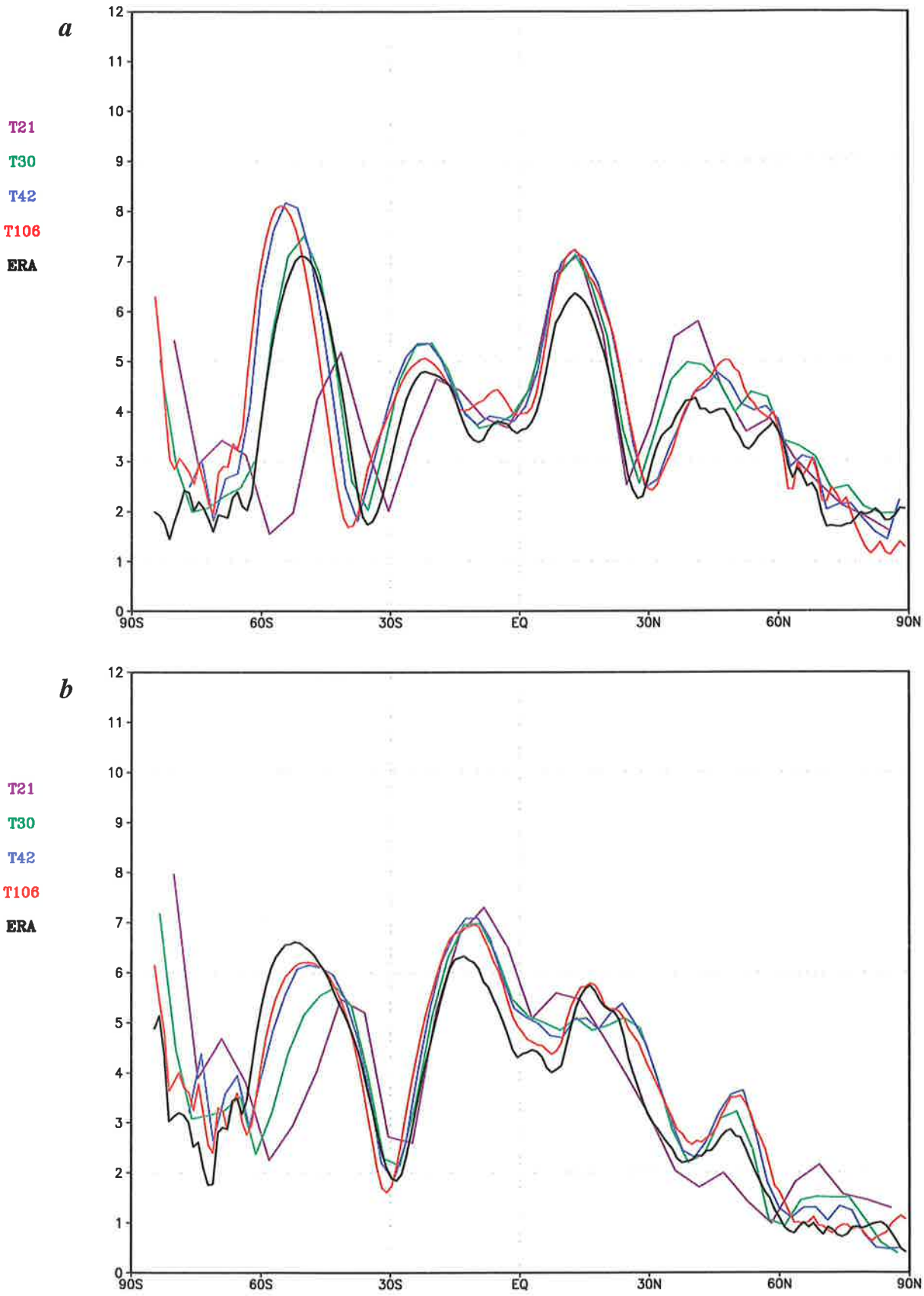

Fig. 13: 10 m wind speed over the oceans for model resolutions T21, T30, T42, T106 and for the ECMWF reanalysis (a) for boreal winter (DJF) and (b) for boreal summer (JJA).

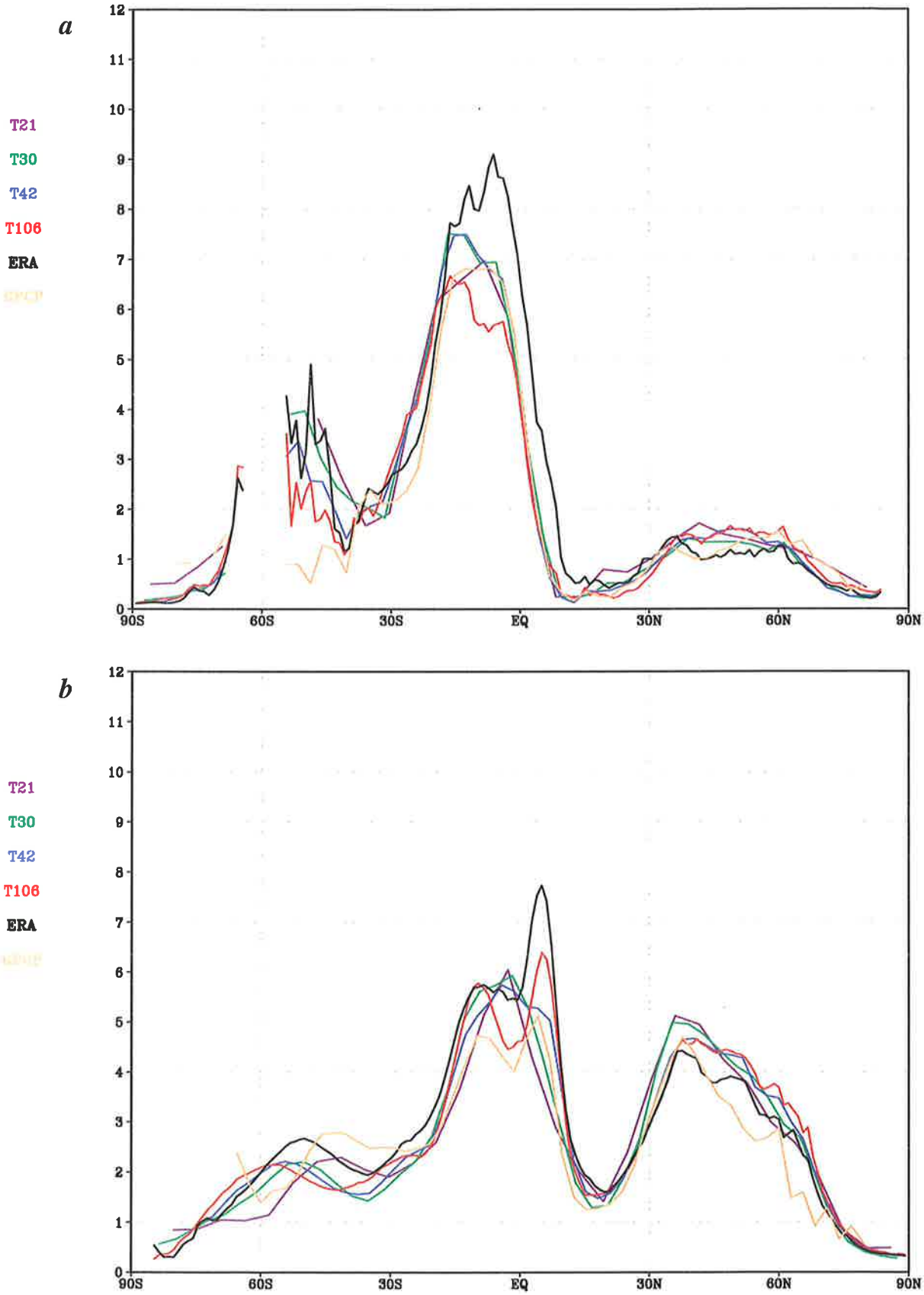

Fig. 14: Zonal mean precipitation for model resolutions T21, T30, T42, T106, for the ECMWF reanalysis and for the GPCP analysis in boreal winter (DJF) (a) over land and (b) over the oceans and in boreal summer (JJA) (c) over land and (d) over the oceans.

c

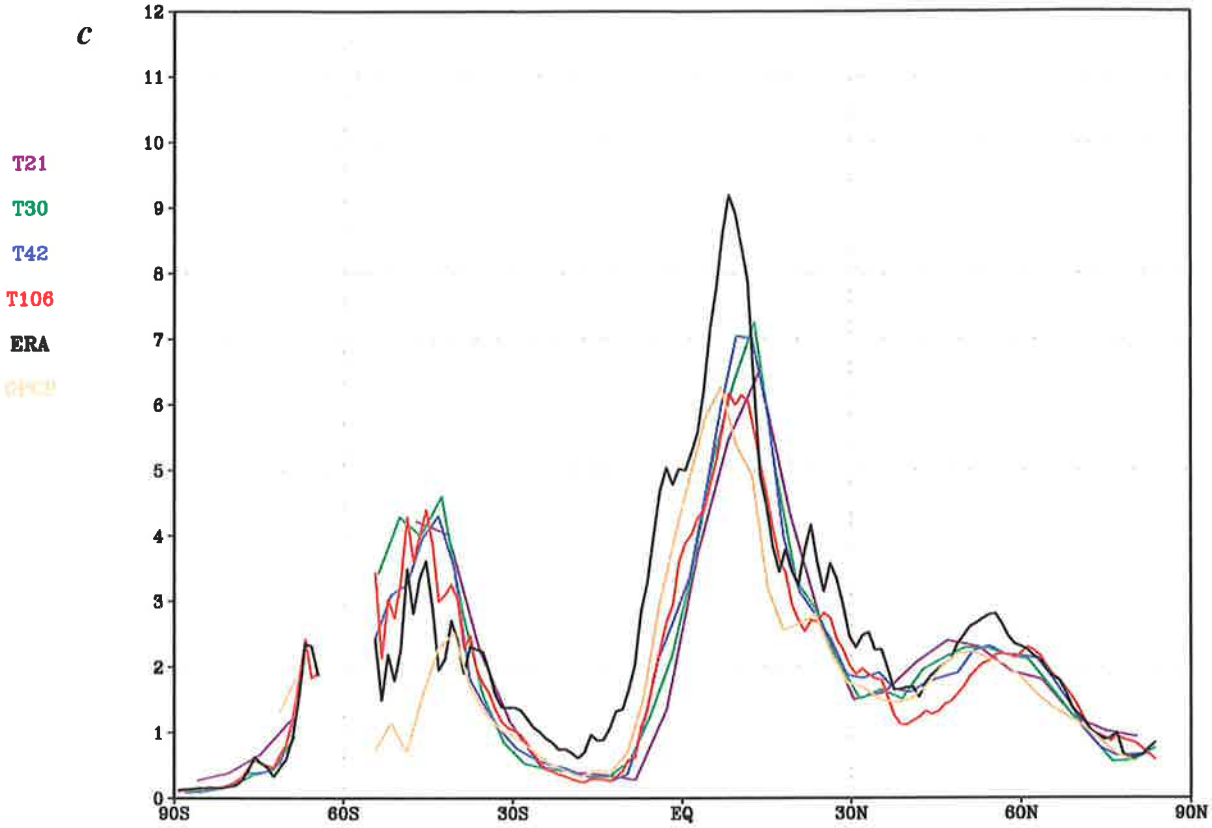
T21
T30
T42
T106
ERA
12
11
10
9
8
7
6
5
4
3
2
1
0
90S
60S
30S
EQ
30N
60N
90N

d

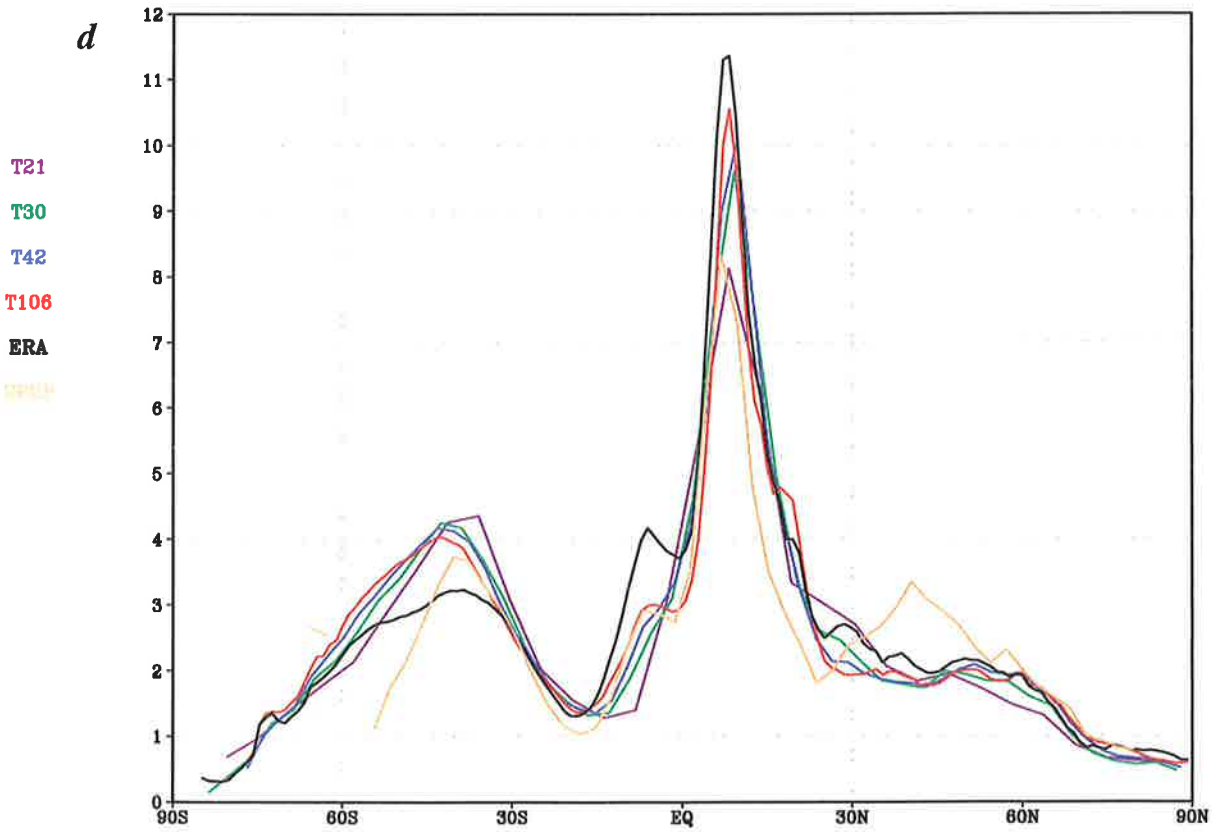
T21
T30
T42
T106
ERA
12
11
10
9
8
7
6
5
4
3
2
1
0
90S
60S
30S
EQ
30N
60N
90N

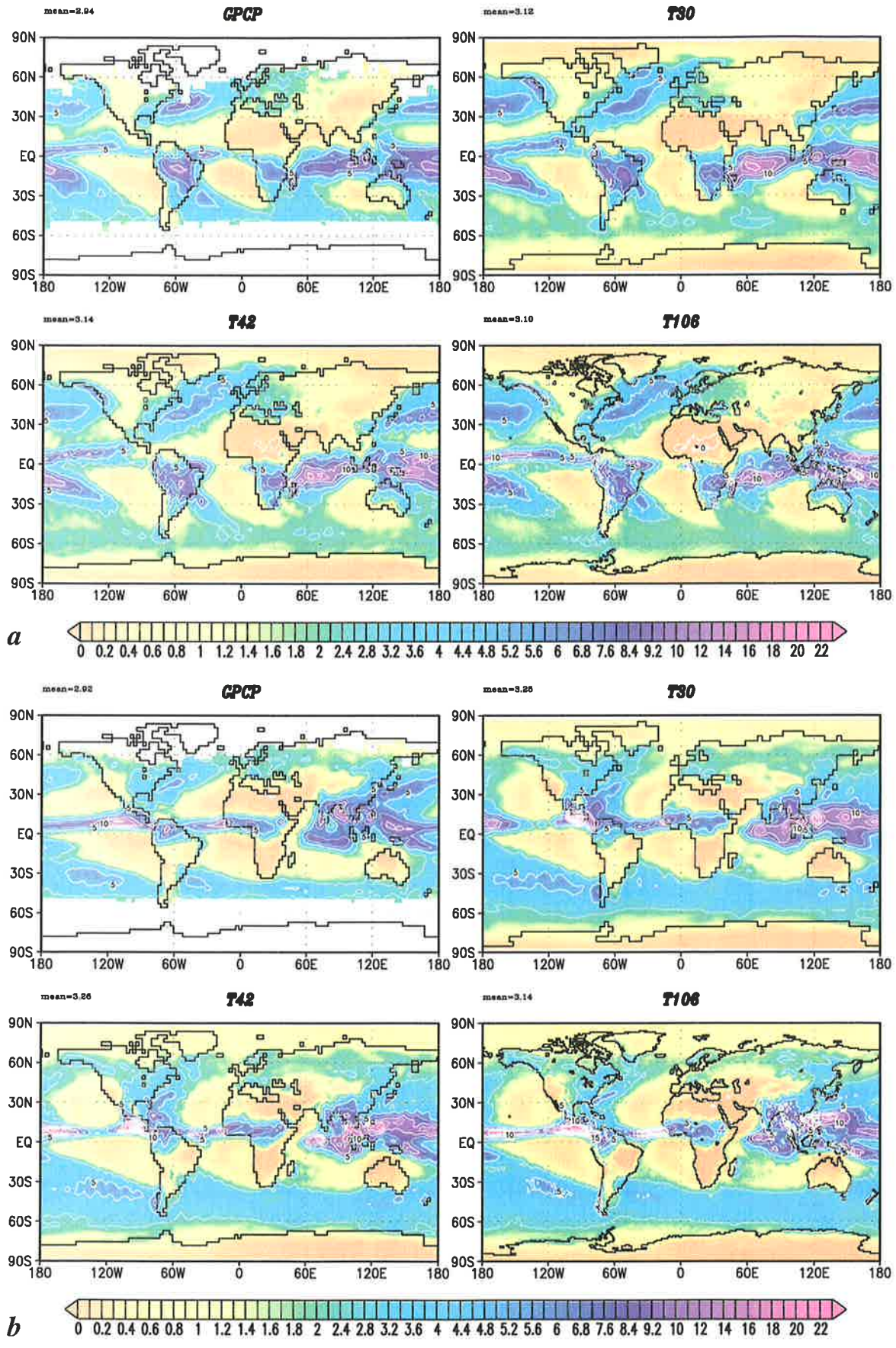

Fig. 15: Global precipitation for GPCP analysis and model resolutions of T30, T42 and T106 (a) for boreal winter (DJF) and (b) for boreal summer (JJA). Contour interval 2.5 mm day^{-1}.

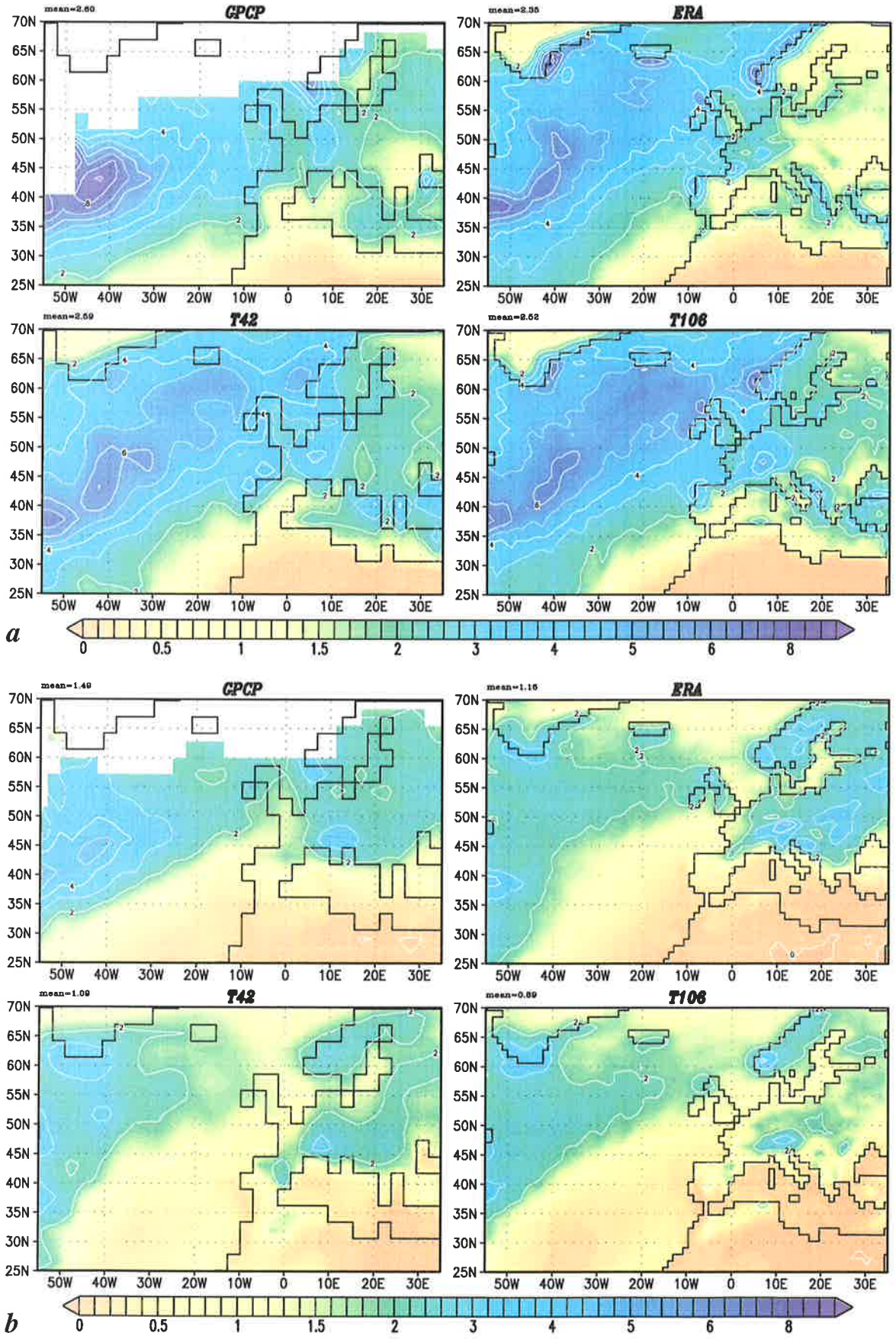

Fig. 16: Precipitation over Europe for GPCP analysis, ECMWF reanalysis and model resolutions of T42 and T106 (a) for boreal winter (DJF) and (b) for boreal summer (JJA). Contour interval 1 mm day^{-1}.

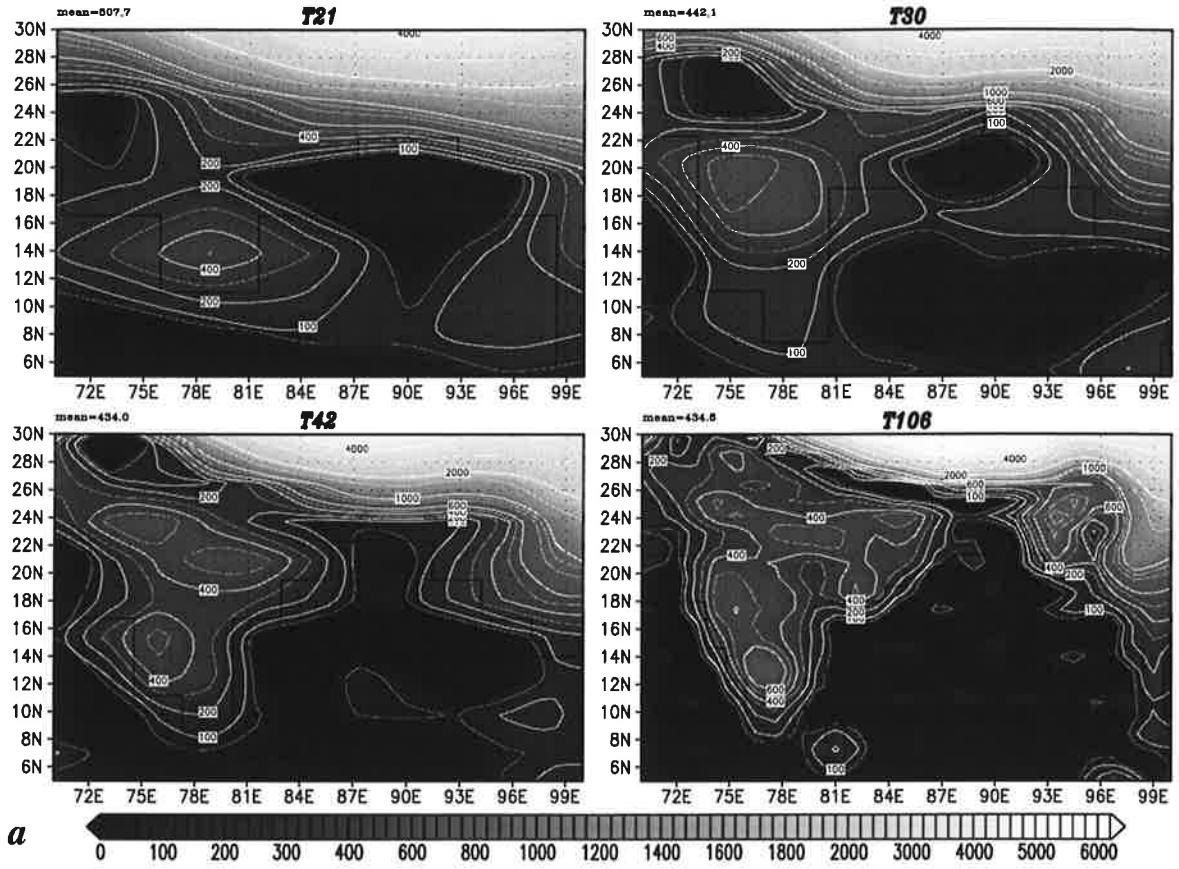

Fig. 17: (a) Orography over India for different ECHAM4 resolutions. Contours at 50, 100, 200, 300, 400, 500, 600, 800, 1000, 1500, 2000 and then every 1000 m. (b) Summer (JJA) precipitation over India for GPCP analysis and three different model resolutions. Contour interval 2 mm day^{-1}. (c) Streamlines and 10m wind convergence (coloured) for ECMWF reanalysis and three different model resolutions.

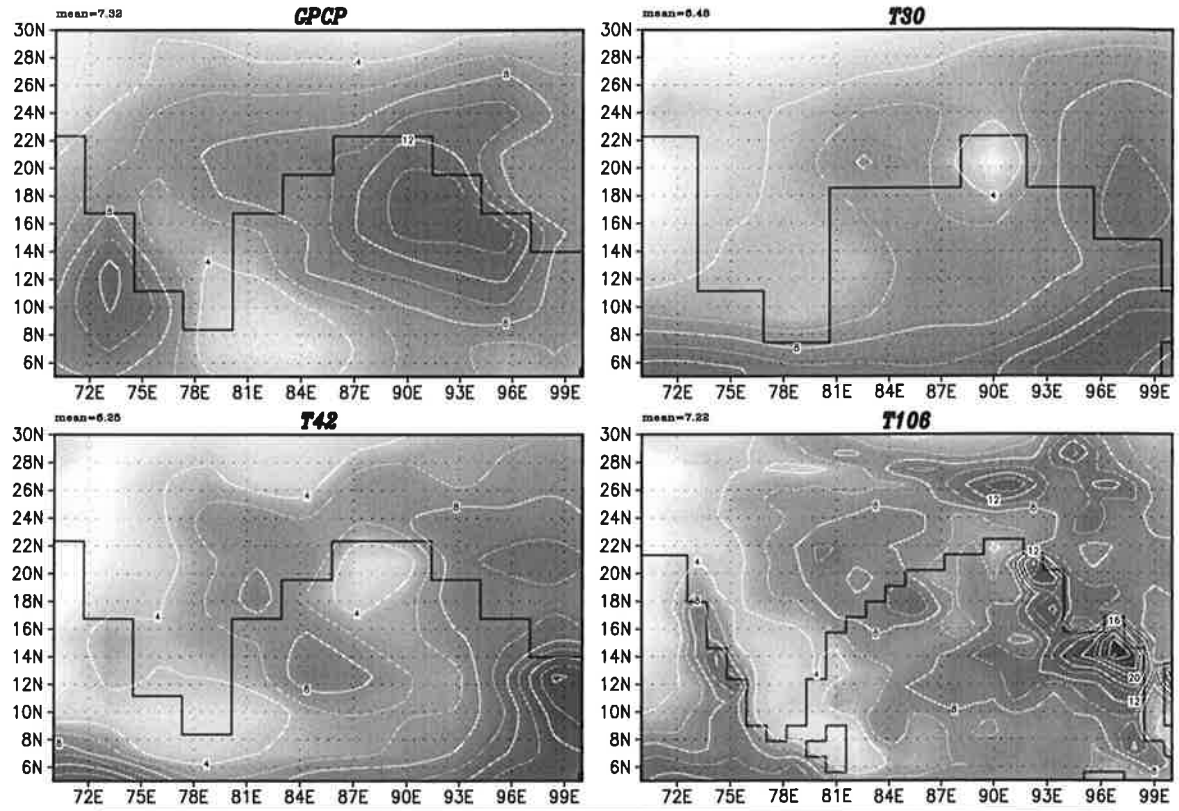
mean=7.32
GPCP
mean=6.46
T30
mean=6.25
T42
mean=7.22
T106
30N 28N 26N 24N 22N 20N 18N 16N 14N 12N 10N 8N 6N
72E 75E 78E 81E 84E 87E 90E 93E 96E 99E
b
1 1.2 1.4 1.6 1.8 2 2.4 2.8 3.2 3.6 4 4.4 4.8 5.2 5.6 6 6.8 7.6 8.4 9.2 10 12 14 16 18 20 22 24 26 28 30

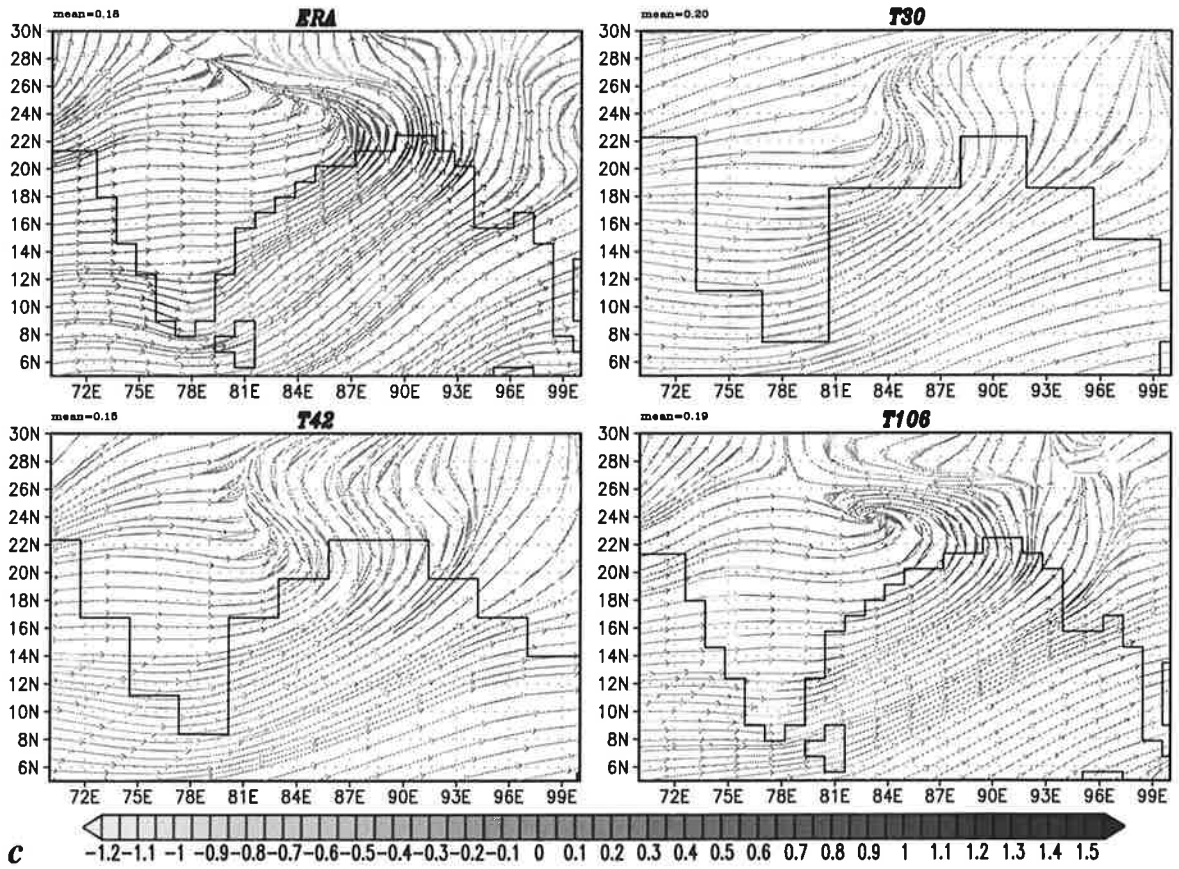
mean=0.18
ERA
mean=0.20
T30
mean=0.15
T42
mean=0.19
T106
30N 28N 26N 24N 22N 20N 18N 16N 14N 12N 10N 8N 6N
72E 75E 78E 81E 84E 87E 90E 93E 96E 99E
c
-1.2 -1.1 -1 -0.9 -0.8 -0.7 -0.6 -0.5 -0.4 -0.3 -0.2 -0.1 0 0.1 0.2 0.3 0.4 0.5 0.6 0.7 0.8 0.9 1 1.1 1.2 1.3 1.4 1.5

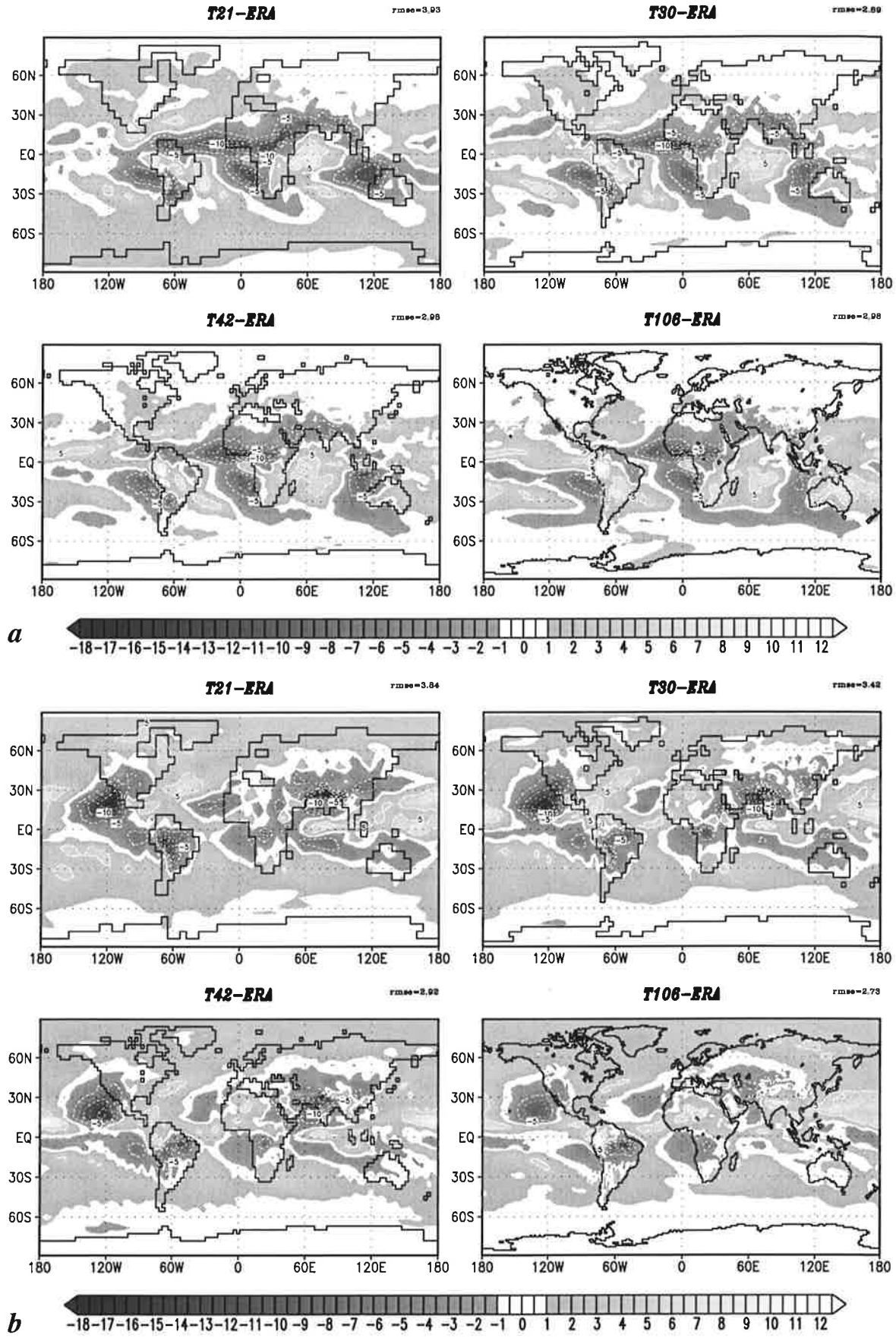

Fig. 18: Total precipitable water errors for different ECHAM4 model resolutions (a) for boreal winter (DJF) and (b) for boreal summer (JJA). Contour interval 2 mm, zero line omitted.

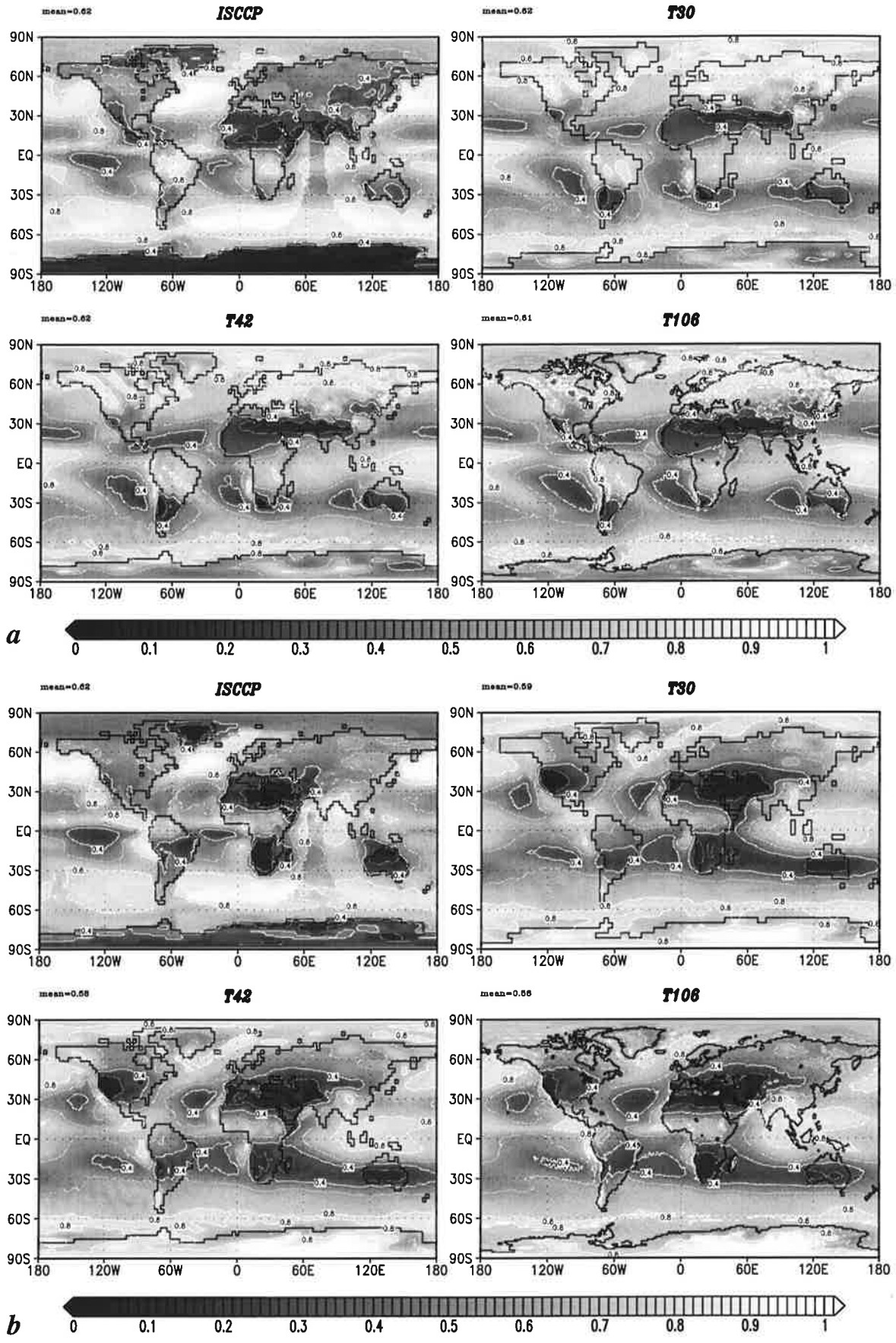

Fig. 19: Total cloud cover from ISCCP analysis and from different ECHAM4 model resolutions (a) for boreal winter (DJF) and (b) for boreal summer (JJA). Contour interval 0.2.

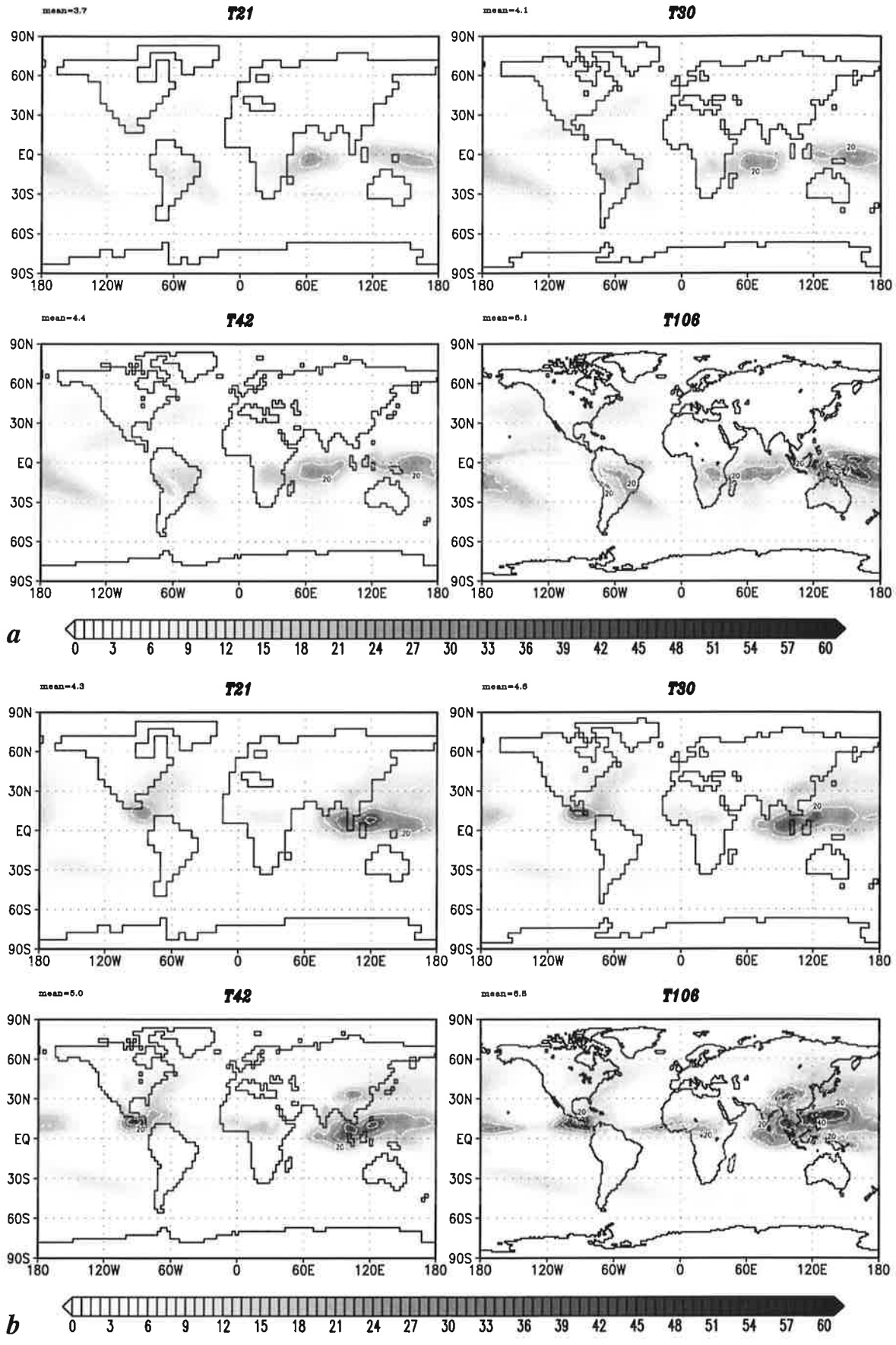

Fig. 20: 250 hPa cloud ice content for ECHAM4 resolutions of T21, T30, T42 and T106 (a) in boreal winter (DJF) and (b) in boreal summer (JJA). Contour interval $5 \cdot 10^{-3}$ g kg^{-1}.

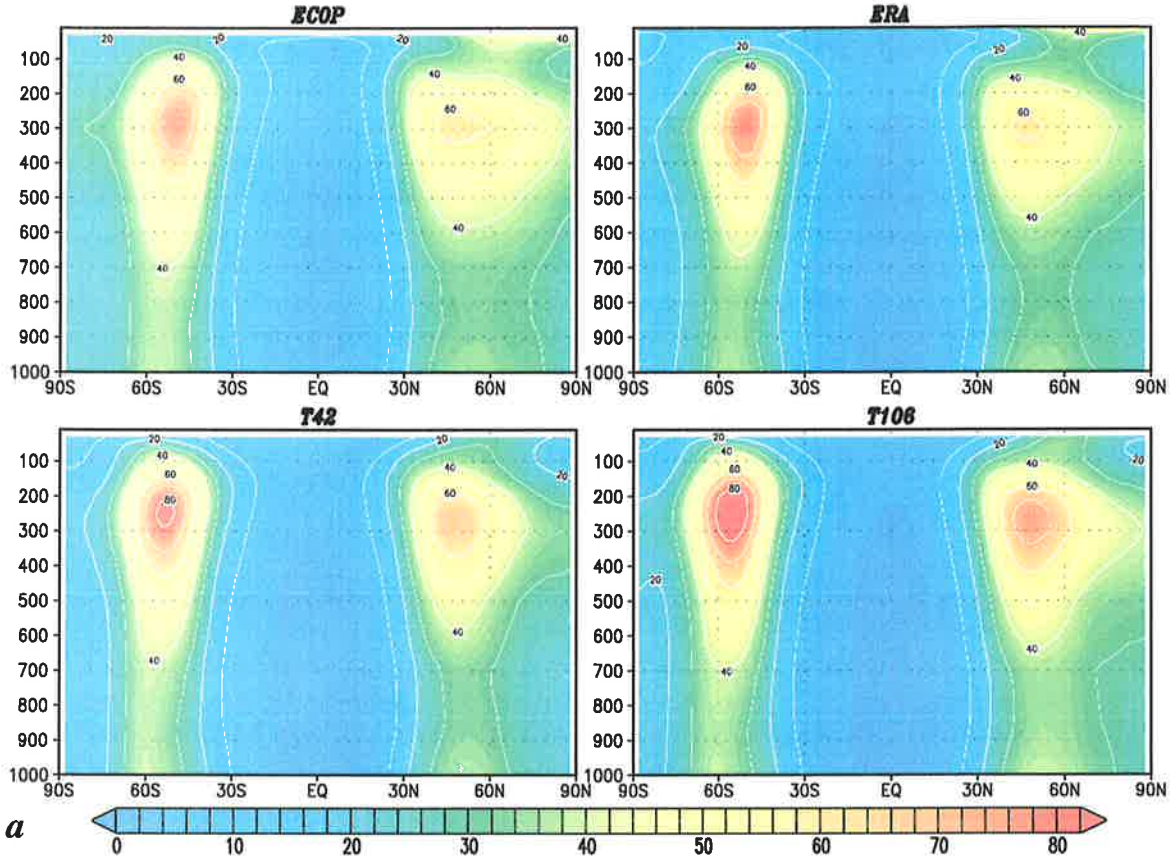
ECOP
ERA
T42
T106
100
200
300
400
500
600
700
800
900
1000
90S
60S
30S
EQ
30N
60N
90N
0
10
20
30
40
50
60
70
80

a

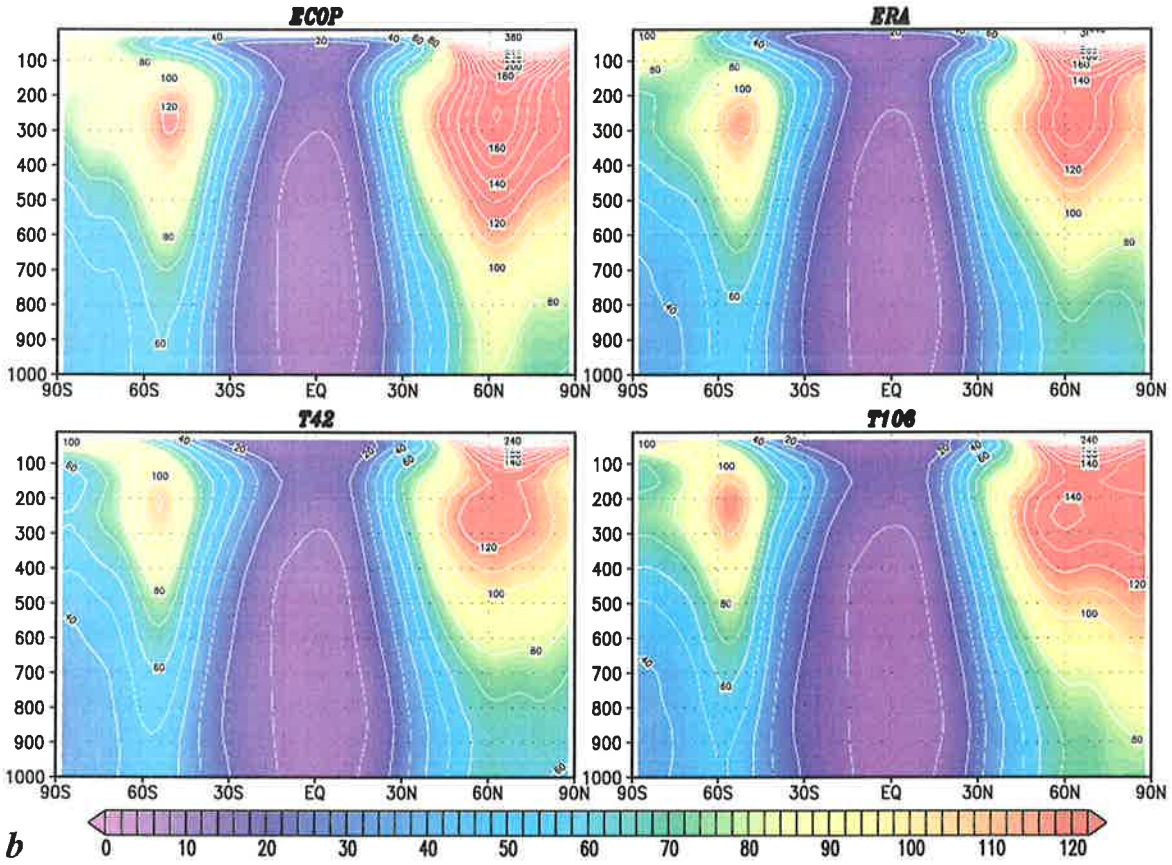
ECOP
ERA
T42
T106
100
200
300
400
500
600
700
800
900
1000
90S
60S
30S
EQ
30N
60N
90N
0
10
20
30
40
50
60
70
80
90
100
110
120

b

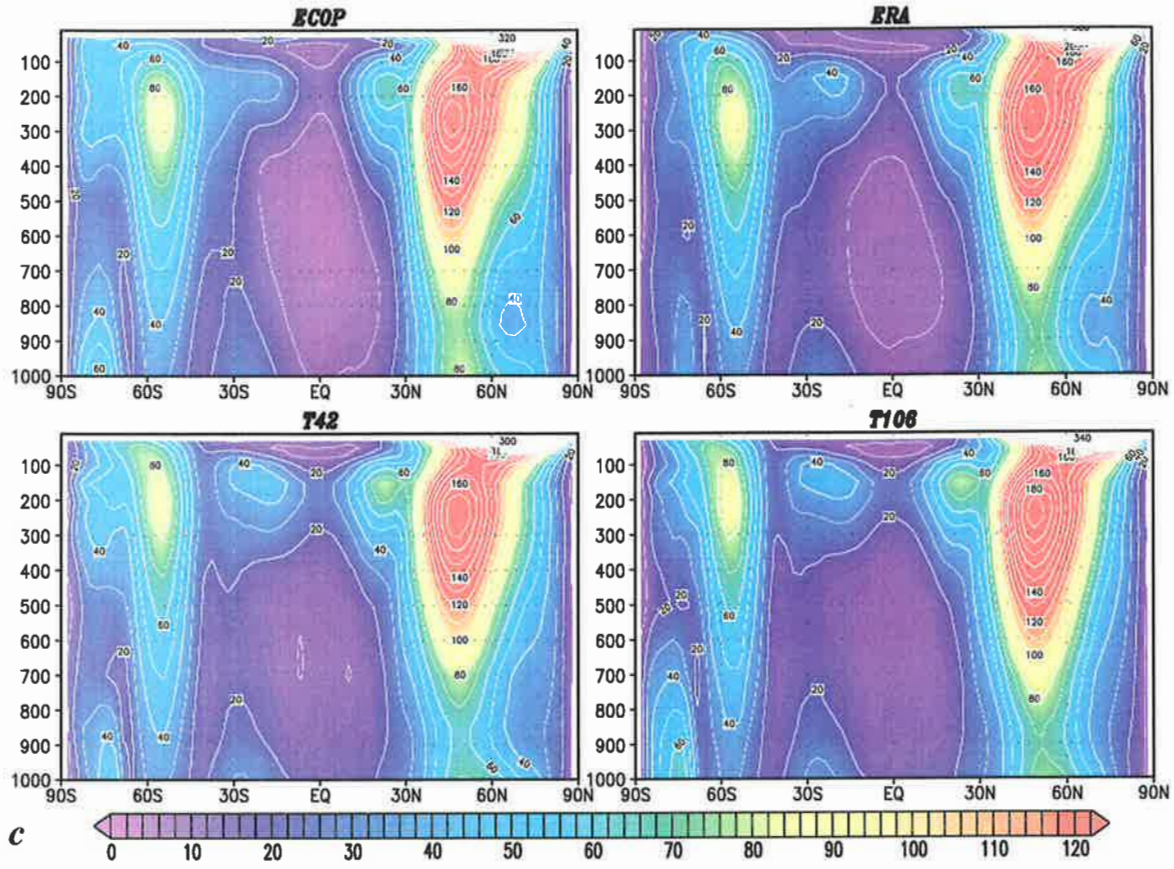

Fig. 21: Latitude-pressure cross sections of the zonal mean standard deviations of geopotential height [gpm] for ECMWF operational analyses (ECOP), ECMWF reanalyses (ERA) and model simulations with T42 and T106 resolution in boreal winter (DJF) by transient eddies (a) in the bandpass regime and (b) in the lowpass regime and (c) by stationary eddies. Contour interval 10 m.

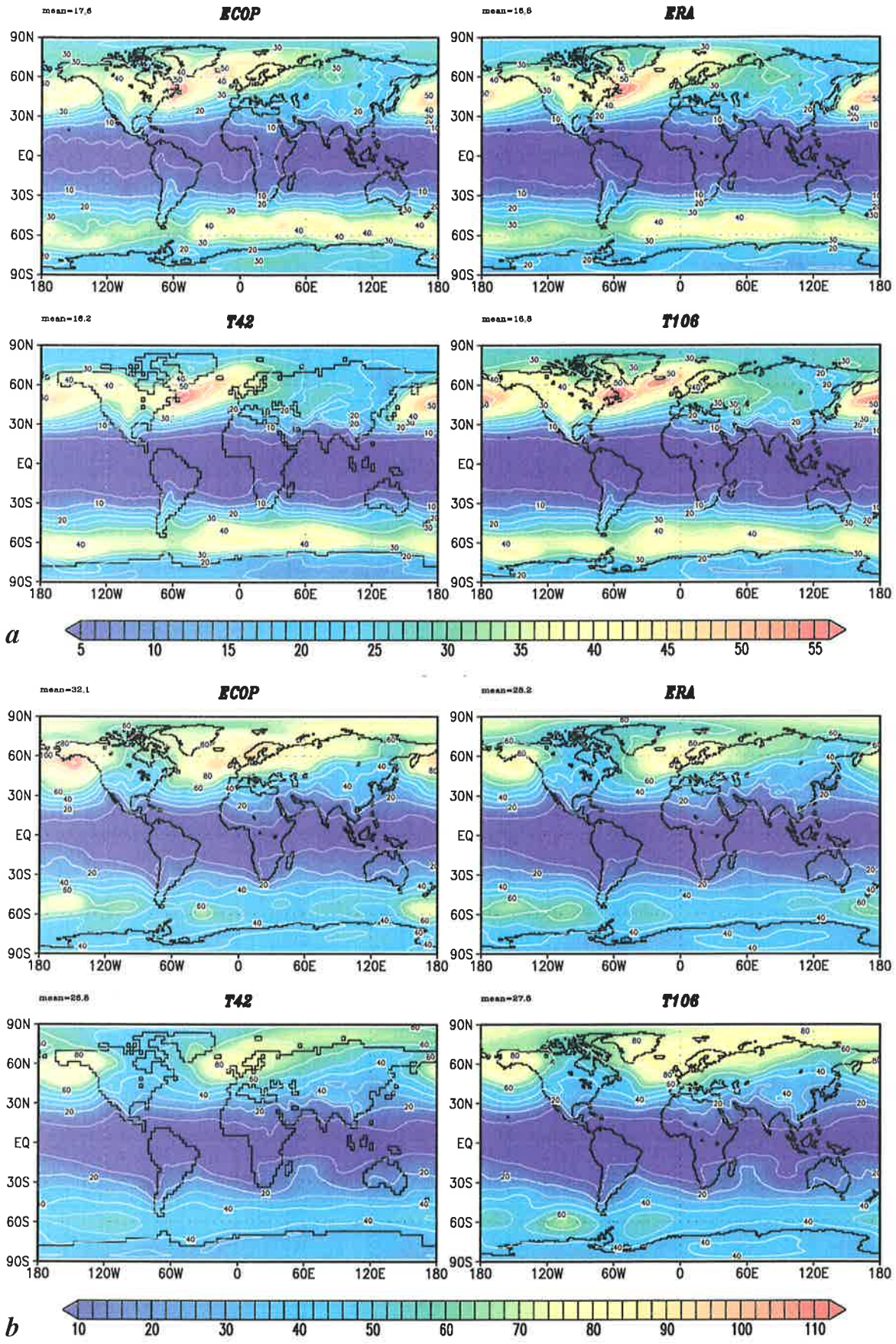

Fig. 22: Standard deviation of 1000 hPa geopotential height [gpm] in boreal winter (DJF) by transient eddies (a) in the bandpass regime (contour interval 5 m) and (b) in the lowpass regime (contour interval 10 m).

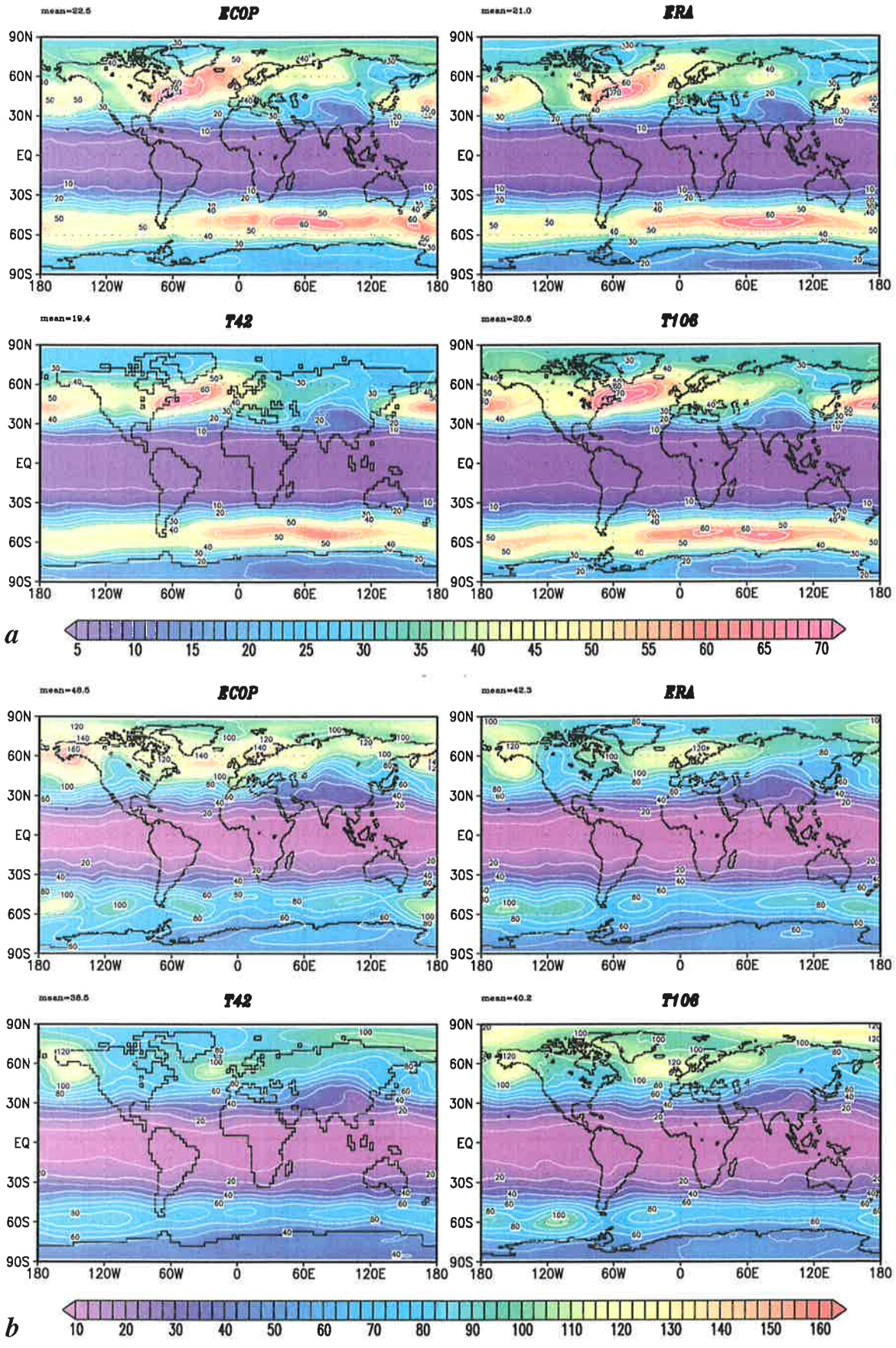

Fig. 23: As Fig. 22, for 500 hPa.

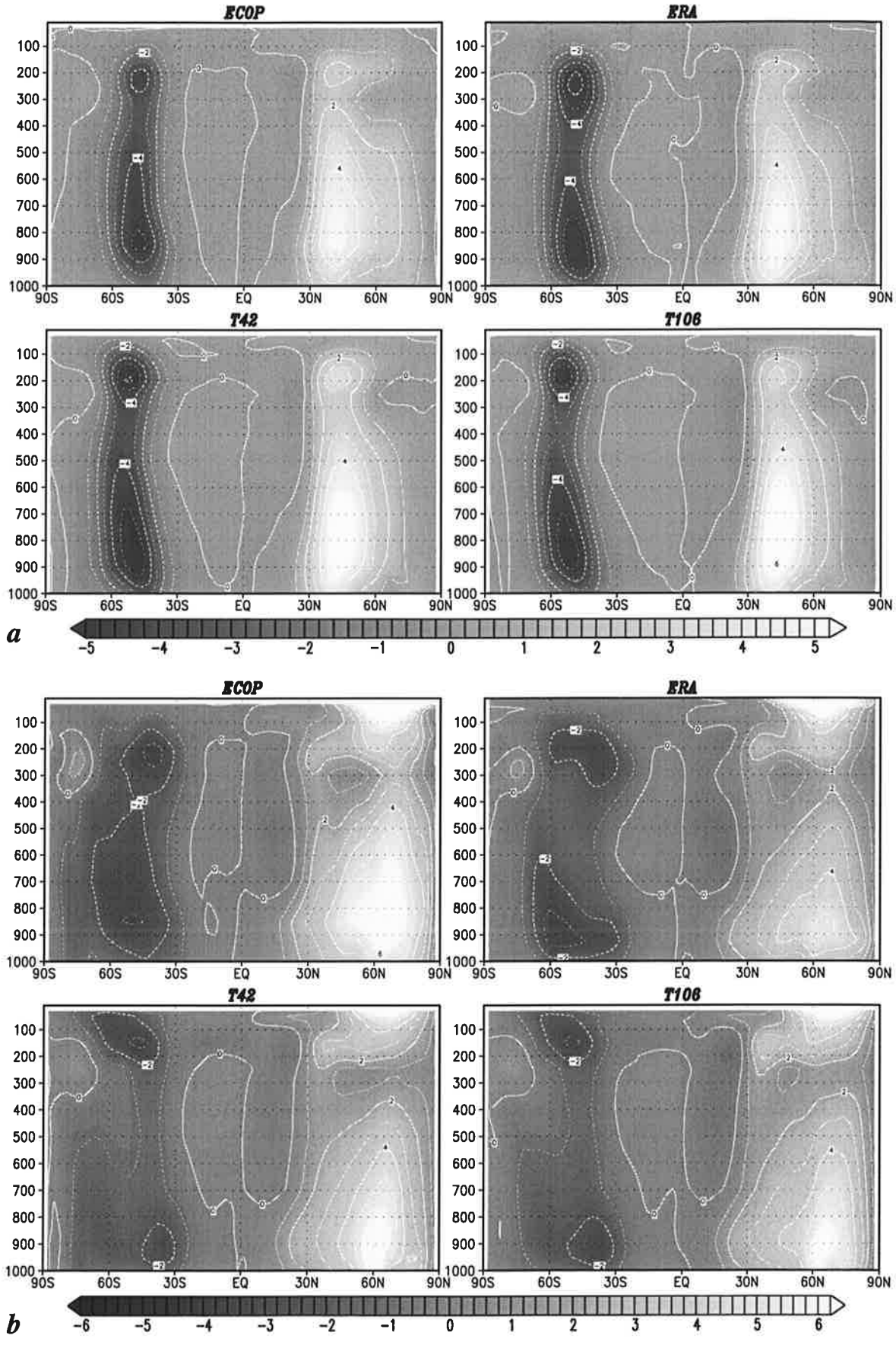
ECOP
ERA
T42
T106
100
200
300
400
500
600
700
800
900
1000
90S
60S
30S
EQ
30N
60N
90N
a
-5
-4
-3
-2
-1
0
1
2
3
4
5
b
-6
-5
-4
-3
-2
-1
0
1
2
3
4
5
6

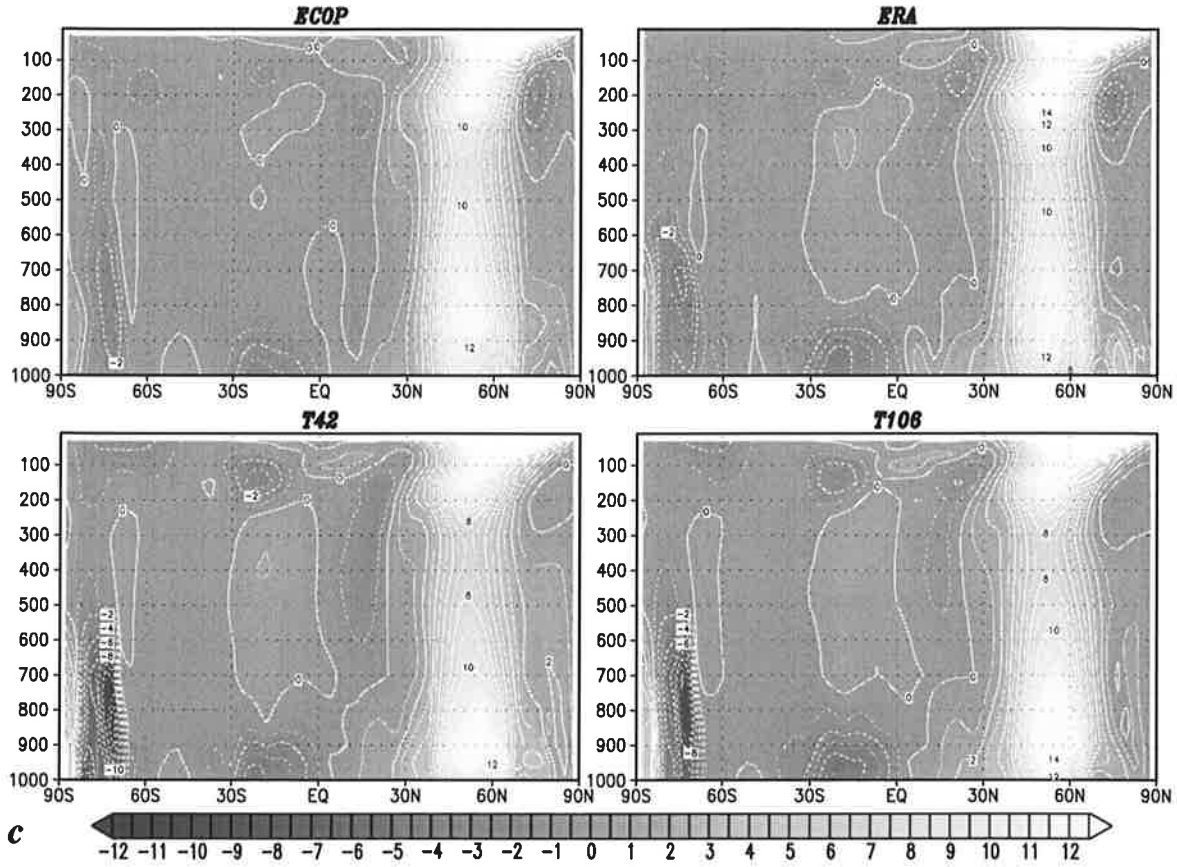

Fig. 24: As Fig. 21, for zonal mean northward transport of sensible heat [K ms^{-1}]. Contour interval 1 K ms^{-1}.

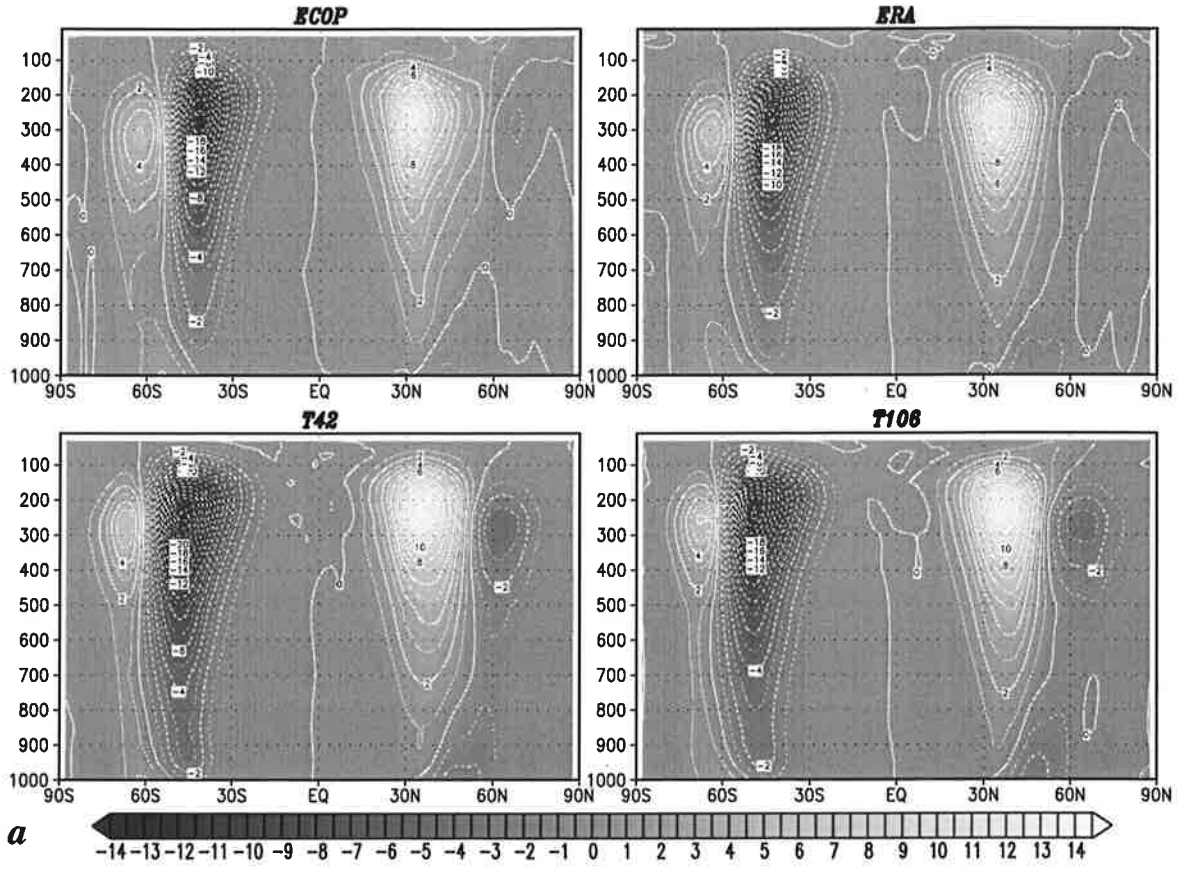
ECOP
ERA
T42
T106
100
200
300
400
500
600
700
800
900
1000
90S
60S
30S
EQ
30N
60N
90N
-14 -13 -12 -11 -10 -9 -8 -7 -6 -5 -4 -3 -2 -1 0 1 2 3 4 5 6 7 8 9 10 11 12 13 14

a

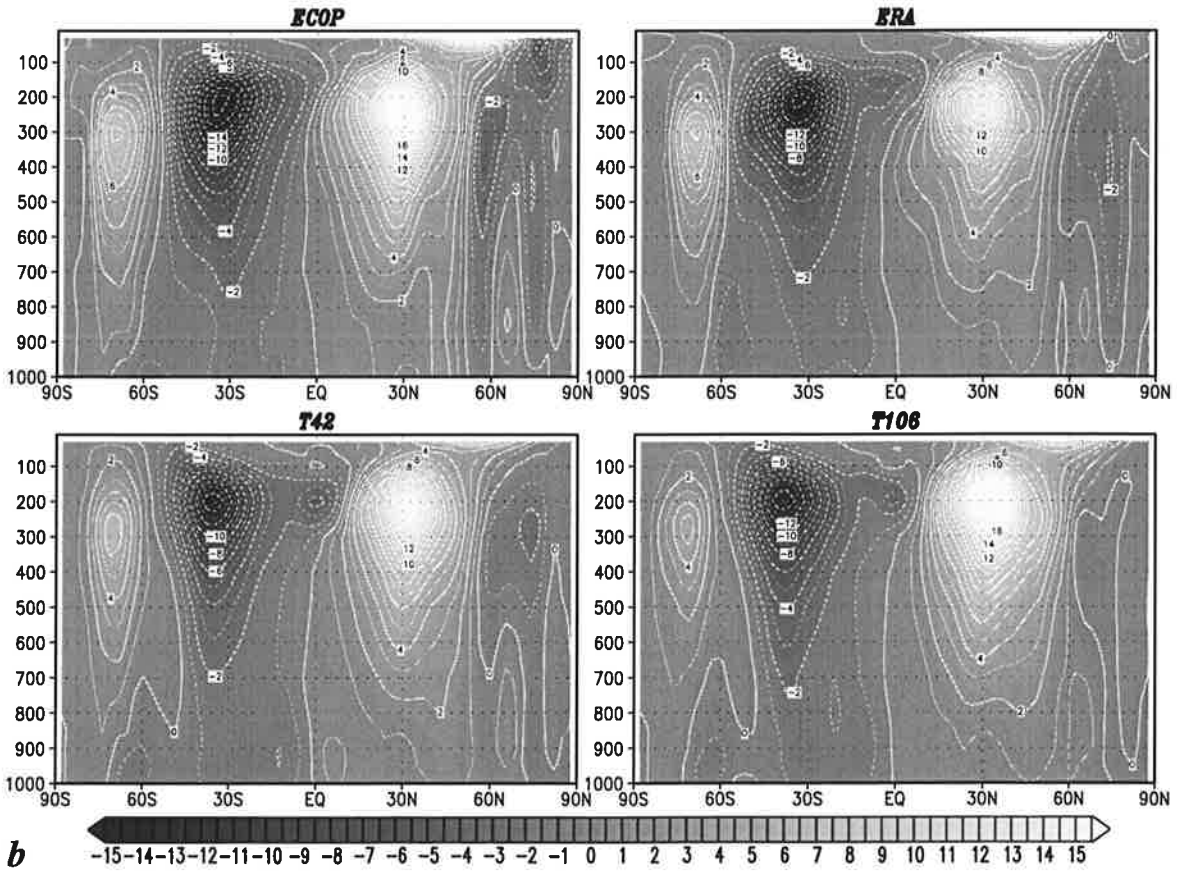
ECOP
ERA
T42
T106
100
200
300
400
500
600
700
800
900
1000
90S
60S
30S
EQ
30N
60N
90N
-15 -14 -13 -12 -11 -10 -9 -8 -7 -6 -5 -4 -3 -2 -1 0 1 2 3 4 5 6 7 8 9 10 11 12 13 14 15

b

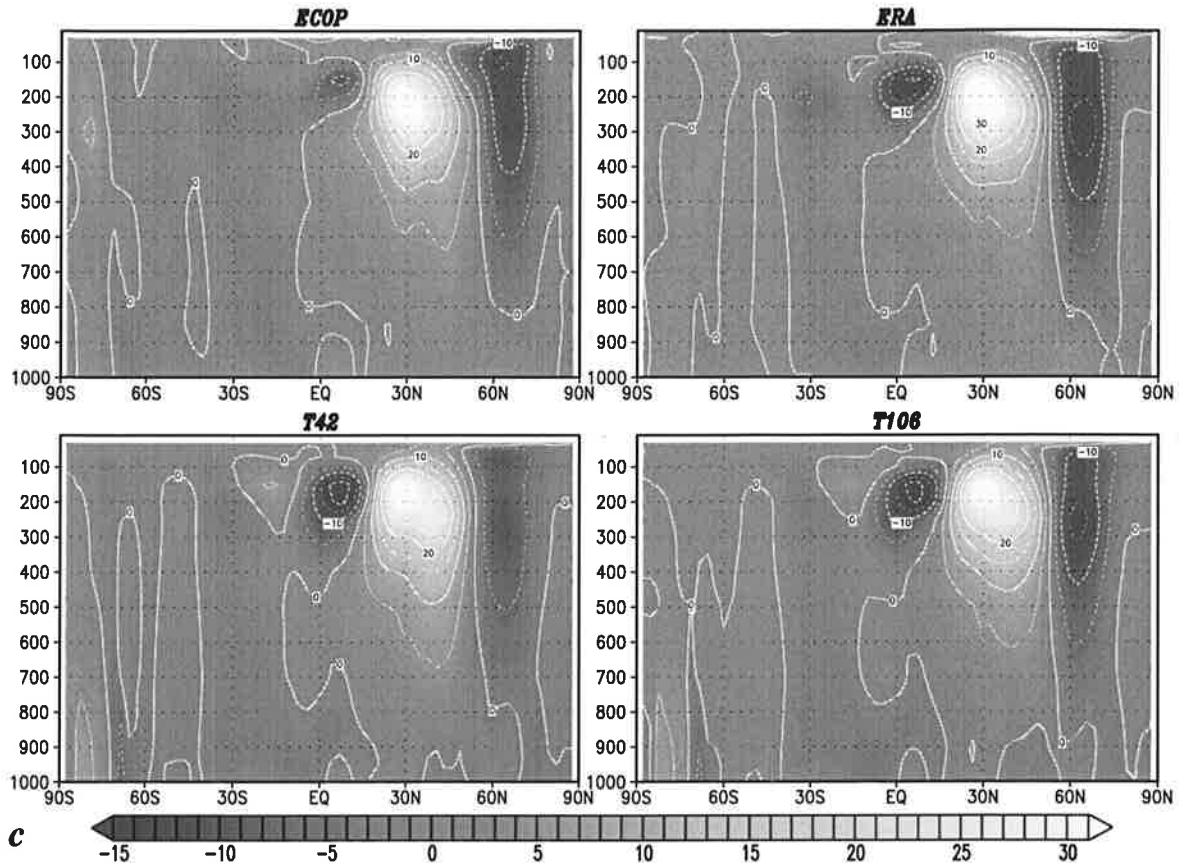

Fig. 25: As Fig. 21, for zonal mean northward transport of westerly momentum [m^2s^{-2}]. Contour interval is 1 m^2s^{-2} for the transient eddies and 5 m^2s^{-2} for the stationary eddies.

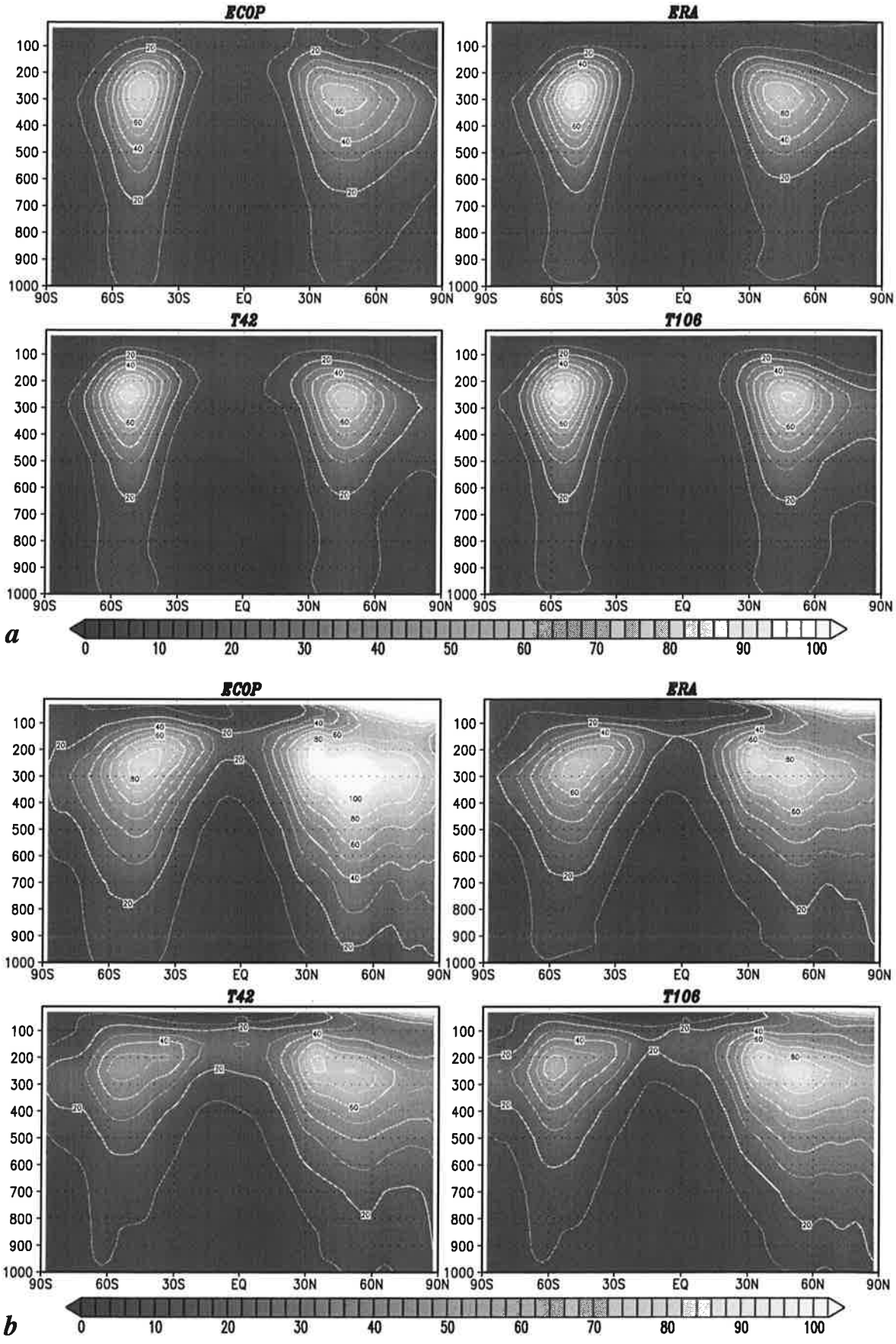
ECOP
ERA
T42
T106
100
200
300
400
500
600
700
800
900
1000
90S
60S
30S
EQ
30N
60N
90N
0
10
20
30
40
50
60
70
80
90
100
a
b

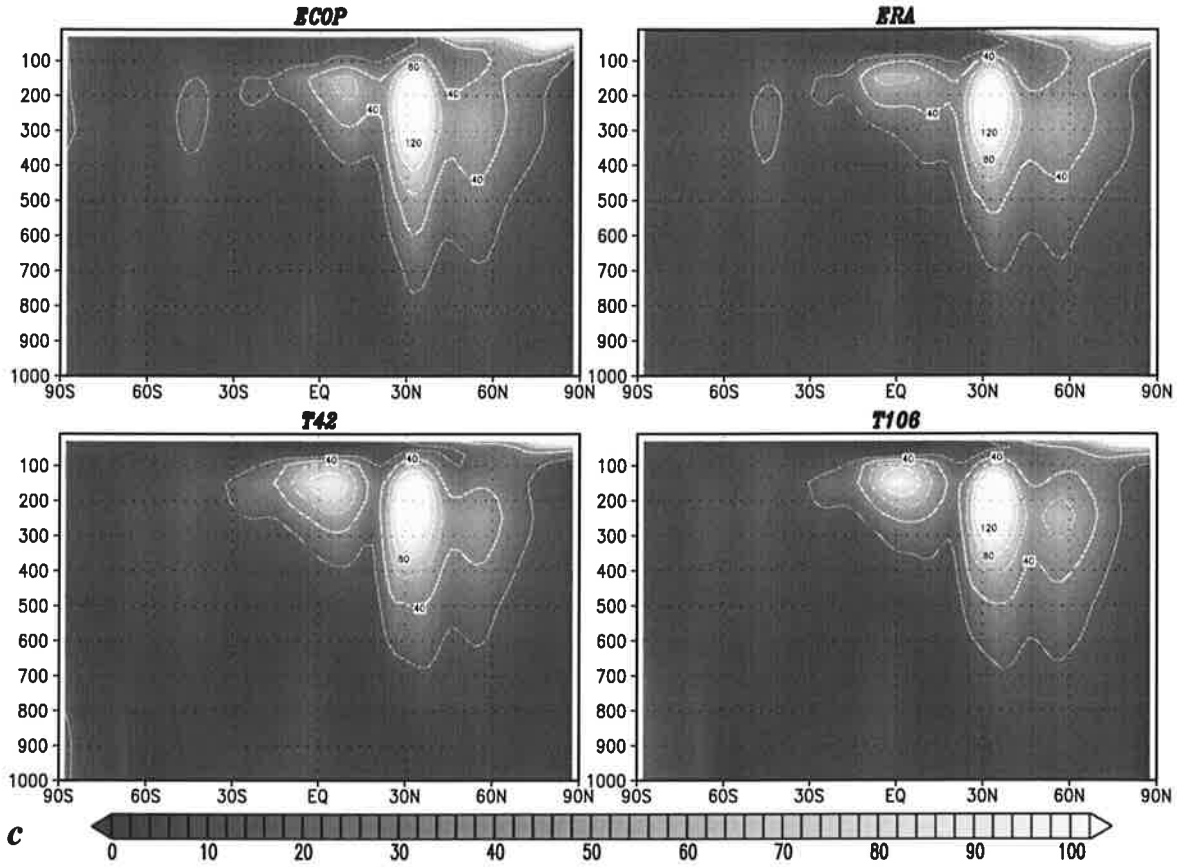

Fig. 26: Latitude-height sections of zonal mean kinetic energy [m^2s^{-2}] in boreal winter (DJF) by transient eddies (a) in the bandpass regime (contour interval 10 m^2s^{-2}) and (b) in the lowpass regime (contour interval 10 m^2s^{-2}) and (c) stationary eddy kinetic energy (contour interval 20 m^2s^{-2}) for ECMWF operational analyses (ECOP) ECMWF reanalyses (ERA) and model simulations with resolution T42 and T106.